TOPICAL REVIEW • OPEN ACCESS

Case studies of electrical characterisation of graphene by terahertz time-domain spectroscopy

To cite this article: Patrick R Whelan *et al* 2021 *2D Mater.* **8** 022003

View the article online for updates and enhancements.

You may also like

- In Situ X-ray Absorption Study of $0.3Li_2MnO_3 \cdot 0.7Li[Mn_xNi_yCo_z]O_2$ Cathode Material for Lithium Rechargeable Battery
Tatiana I. Nedoseykina, Min Gyu Kim and Youngil Lee
- Microfabricated ratchet structures for concentrating and patterning motile bacterial cells
Sang Yub Kim, Eun Se Lee, Ho Jae Lee et al.
- In Situ XAFS Study of $LiMn_{0.6}Fe_{0.4}PO_4$ Cathode Material for Lithium Rechargeable Battery
Tatiana I. Nedoseykina, Min Gyu Kim and Youngil Lee



This content was downloaded from IP address 129.175.97.14 on 28/10/2021 at 20:17

2D Materials

TOPICAL REVIEW

Case studies of electrical characterisation of graphene by terahertz time-domain spectroscopy

Patrick R Whelan[1,2], Binbin Zhou[3], Odile Bezencenet[4], Abhay Shivayogimath[1,2], Neeraj Mishra[5,6], Qian Shen[3,7,8], Bjarke S Jessen[1,2,9,10], Iwona Pasternak[11,12], David M A Mackenzie[13], Jie Ji[1,2], Cunzhi Sun[1,2], Pierre Seneor[14], Bruno Dlubak[14], Birong Luo[15], Frederik W Østerberg[16], Deping Huang[17], Haofei Shi[17], Da Luo[18], Meihui Wang[18,19], Rodney S Ruoff[18,19,20,21], Ben R Conran[22], Clifford McAleese[22], Cedric Huyghebaert[23], Steven Brems[23], Timothy J Booth[1,2], Ilargi Napal[24], Wlodek Strupinski[11,12], Dirch H Petersen[25], Stiven Forti[5], Camilla Coletti[5,6], Alexandre Jouvray[22], Kenneth B K Teo[22], Alba Centeno[24], Amaia Zurutuza[24], Pierre Legagneux[4], Peter U Jepsen[2,3] and Peter Bøggild[1,2]

1 DTU Physics, Technical University of Denmark, Fysikvej, Bld. 309, DK-2800 Kgs. Lyngby, Denmark
2 Centre for Nanostructured Graphene (CNG), Technical University of Denmark, Ørsteds Plads 345C, DK-2800 Kgs. Lyngby, Denmark
3 DTU Fotonik, Technical University of Denmark, Ørsteds Plads 343, DK-2800 Kongens Lyngby, Denmark
4 Thales Research and Technology, 91767 Palaiseau, France
5 CNI@NEST, Istituto Italiano di Tecnologia, Piazza San Silvestro 12, 56127 Pisa, Italy
6 Graphene Labs, Istituto Italiano di Tecnologia, Via Morego 30, 16163 Genova, Italy
7 School of Information Engineering, Nanchang University, Nanchang 330031, People's Republic of China
8 College of Science, Zhejiang University of Technology, Hangzhou 310014, People's Republic of China
9 Department of Physics, Columbia University, New York, NY 10027, United States of America
10 Department of Mechanical Engineering, Columbia University, New York, NY 10027, United States of America
11 Faculty of Physics, Warsaw University of Technology, Koszykowa 75, 00-662 Warsaw, Poland
12 Vigo System S.A., 129/133 Poznanska Str, 05-850 Ozarow Mazowiecki, Poland
13 Department of Electronics and Nanoengineering, Aalto University, Box 13500, FI-00076 Aalto, Finland
14 Unité Mixte de Physique, CNRS, Thales, Université Paris-Saclay, 91767 Palaiseau, France
15 College of Physics and Materials Science, Tianjin Normal University, 300387 Tianjin, People's Republic of China
16 CAPRES—A KLA Company, Scion-DTU, Bld. 373, DK-2800 Kgs. Lyngby, Denmark
17 Chongqing Institute of Green and Intelligent Technology, Chinese Academy of Sciences, 266 Fang Zheng Ave., Chongqing 400714, People's Republic of China
18 Center for Multidimensional Carbon Materials (CMCM), Institute for Basic Science (IBS), Ulsan 44919, Republic of Korea
19 Department of Chemistry, Ulsan National Institute of Science and Technology (UNIST), Ulsan 44919, Republic of Korea
20 Department of Materials Science and Engineering, Ulsan National Institute of Science and Technology (UNIST), Ulsan 44919, Republic of Korea
21 School of Energy and Chemical Engineering, Ulsan National Institute of Science and Technology (UNIST), Ulsan 44919, Republic of Korea
22 AIXTRON Ltd, Buckingway Business Park, Anderson Road, Swavesey, Cambridge CB24 4FQ, United Kingdom
23 IMEC vzw, Kapeldreef 75, BE-3001 Leuven, Belgium
24 Graphenea Semiconductor S.L.U, Paseo Mikeletegi 83, 20009 San Sebastian, Spain
25 DTU Energy, Technical University of Denmark, Fysikvej, Bld. 310, DK-2800 Kgs. Lyngby, Denmark

E-mail: pbog@dtu.dk

Keywords: terahertz spectroscopy, large-scale graphene, CVD graphene, electrical mapping

OPEN ACCESS

RECEIVED
29 October 2020

REVISED
20 November 2020

ACCEPTED FOR PUBLICATION
14 January 2021

PUBLISHED
17 February 2021

Original content from this work may be used under the terms of the Creative Commons Attribution 4.0 licence.

Any further distribution of this work must maintain attribution to the author(s) and the title of the work, journal citation and DOI.

Abstract

Graphene metrology needs to keep up with the fast pace of developments in graphene growth and transfer. Terahertz time-domain spectroscopy (THz-TDS) is a non-contact, fast, and non-destructive characterization technique for mapping the electrical properties of graphene. Here we show several case studies of graphene characterization on a range of different substrates that highlight the versatility of THz-TDS measurements and its relevance for process optimization in graphene production scenarios.

1. Introduction

Large-area, fast, non-destructive, and precise measurement techniques are required as the manufacturing of graphene and graphene technology is scaled up [1]. Rapid developments in graphene growth and transfer demand improved quality control during fabrication. Spatially determining the electrical parameters of a given sample is critical, since electrical inhomogeneities may

© 2021 The Author(s). Published by IOP Publishing Ltd

dramatically reduce the performance of final devices.

Terahertz time-domain spectroscopy (THz-TDS) is a non-contact and non-destructive measurement technique that can spatially map the electrical properties (DC conductivity σ_{DC}, scattering time τ, carrier density n, and mobility μ) of graphene on substrates relevant for the use of graphene such as Si [2–6], quartz [7], SiC [8, 9], sapphire [10], and polymers [11, 12], and is maturing as a metrology tool for characterizing the electrical properties of graphene [1, 13–16]. THz spectroscopy is also applicable for measuring conductivity and scattering processes of other 2D materials such as MoS_2, WSe_2, and VN [17–20].

Here, we evaluate THz-TDS for characterization of graphene in a wide range of different scenarios. This includes optimization of graphene growth, transfer, and post-transfer processing. We will also discuss the possible implementation of real-time THz-TDS in both batch and roll-to-roll (R2R) production of graphene.

The paper is organized as follows. In section 2 we discuss how to perform THz-TDS measurements of graphene and how to analyze THz-TDS data in different cases. Furthermore, we present how to extract electrical and electronic parameters (σ_{DC}, τ, n, μ, renormalized Fermi velocity v_F^*) by fitting the frequency dependent conductivity at THz frequencies with the Drude model. In section 3 we present several case studies of THz-TDS measurements of graphene including encapsulated graphene and THz-TDS for quality control in graphene production scenarios.

2. Methods

THz-TDS measurements were performed with two different setups. The main setup is a commercial fibre-coupled spectrometer (Picometrix T-Ray 4000) with a programmable stage that allows for raster scanning samples in the focal plane of the THz beam and creating spatial maps of the electrical properties of graphene [14]. The setup is capable of measuring within a frequency range of ~0.5–1.5 THz with a spot size of ~400 μm at 1 THz [5]. Measurements were performed with this setup and in transmission-mode if not elsewise stated. The second setup is a custom-built ultra-broadband setup based on two-color femtosecond air-plasma THz generation and an air biased coherent detection scheme [21–23]. This setup covers an extended spectral frequency range up to ~30 THz due to the extremely short pulse duration of a few tens of fs compared to the few-ps duration for the commercial setup as shown in figure 1. For the high-resistivity (HR, $\rho > 10$ kΩ cm) silicon substrates used, the spectral range of reproducible results is limited to approximately 2–10 THz.

2.1. THz-TDS measurement schemes

THz-TDS measurements can be performed in transmission mode or reflection mode as illustrated in figures 1(a)–(c) with examples of measured THz time-domain waveforms for graphene on different substrates shown in figure 1(d). For transmission mode measurements it is a requirement that the substrate is at least partially transparent to THz radiation, with HR Si, SiC, sapphire, and many polymeric materials having been successfully used. The waveforms typically contain several transients that are separated in time, due to internal reflections inside the substrate; a transient $\tilde{E}^{(dir)}$ from the directly transmitted pulse followed by a transient $\tilde{E}^{(1st)}$ from the first internal reflection inside the substrate, a transient $\tilde{E}^{(2nd)}$ from the second internal reflection and so forth. The internal reflections are easily seen in figure 1(d) when HR-Si is used as substrate, while for SiC these internal reflections are not as clear due to the higher absorption in the substrate compared to HR-Si [24, 25]. For thin (up to 400 μm) polymeric substrate (such as polyethylene terephthalate, PET) the transients from directly transmitted pulse and internal reflections may appear as a single reshaped transient, since the thickness and refractive index of the substrate leads to a propagation time within the substrate that is shorter than the THz pulse duration [11]. Due to the short pulse duration of the custom-built air plasma setup it is still possible to measure individual transients for polymer substrates with such a setup [12].

The Fourier transforms of the THz waveforms transmitted through substrate $\tilde{E}_{sub}(\omega)$ and graphene covered substrate $\tilde{E}_{film}(\omega)$ are used to calculate the frequency-dependent complex transmission function $\tilde{T}_{film}(\omega) = \tilde{E}_{film}(\omega)/\tilde{E}_{sub}(\omega)$, from which the complex sheet conductivity of the graphene layer, $\tilde{\sigma}_s(\omega) = \sigma_1 + i\sigma_2$ is obtained. The transmission function is calculated for individual transients by applying window functions. For data acquired with the commercial spectrometer we generally use a cosine tapered (Tukey) window function with 50% taper length (0.5 cosine fraction) and a 2.5 ps width. The window function width and tapering were determined by varying the parameters until small changes did not induce significant re-shaping of the frequency-dependent conductivity.

The means of determining $\tilde{\sigma}_s(\omega)$ from $\tilde{T}_{film}(\omega)$ depends on the transient used for the analysis [14]. For the directly transmitted pulse and the first internal reflection the relations are, respectively,

$$\tilde{\sigma}_s^{(dir)}(\omega) = \frac{n_A}{Z_0}\left(\frac{1}{\tilde{T}_{film}^{(dir)}(\omega)} - 1\right) \quad (1)$$

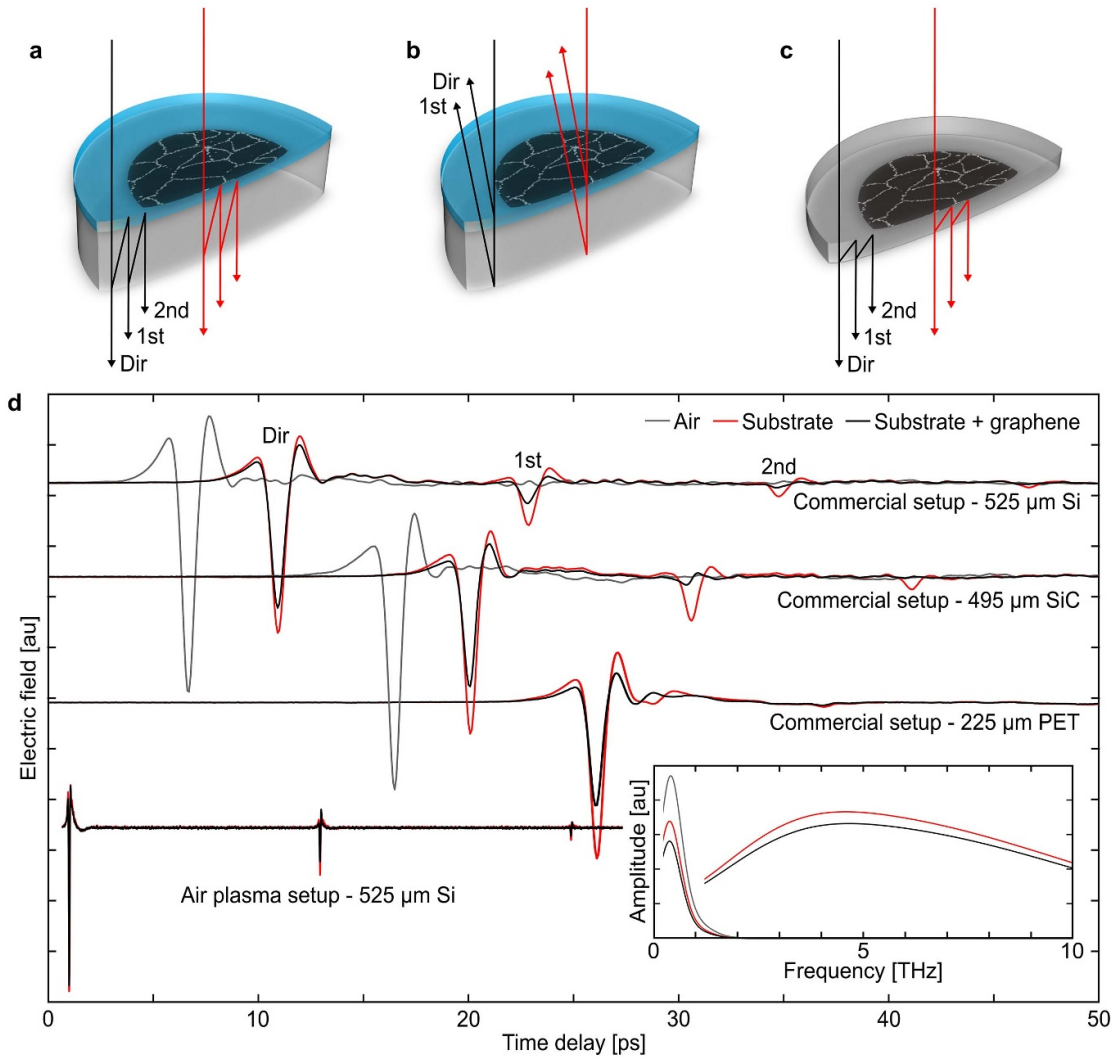


Figure 1. (a)–(c) Illustrations of THz-TDS measurements, (a) transmission mode, (b) reflection mode, and (c) transmission mode for thin substrate. Arrows highlight internal reflections within substrate. (d) Time-domain waveforms acquired in transmission mode for graphene on different substrates with commercial and air plasma setup. Inset shows Fourier transforms of the part of the waveform belonging to the first internal reflection for measurements on 525 μm Si with the commercial and air plasma setups.

$$\tilde{\sigma}_{s}^{(1st)}(\omega) = \frac{n_A\sqrt{n_A^2 + 4n_An_B\tilde{T}_{film}^{(1st)}(\omega) + 4n_B^2\tilde{T}_{film}^{(1st)}(\omega)} - n_A^2 - 2n_An_B\tilde{T}_{film}^{(1st)}(\omega)}{2n_BZ_0\tilde{T}_{film}^{(1st)}(\omega)} \quad (2)$$

where $n_A = \tilde{n}_{sub} + 1$ and $n_B = \tilde{n}_{sub} - 1$ for a substrate with refractive index $\tilde{n}_{sub}$ and Z_0 is the vacuum impedance [14, 26]. The Tinkham relations are used for transmission and reflection coefficients of thin conducting films ($d_{film} \ll \lambda/n_{film}$) [27].

In the case of thin polymeric substrates, where $\tilde{T}_{film}(\omega)$ contains terms from all transmitted transients, $\sigma_s(\omega)$ can be determined as

$$\tilde{\sigma}_{s}^{(all)}(\omega) = \frac{n_A^2 - \tilde{p}^2n_B^2\left(\tilde{p}^2n_B^2 - n_A^2\right)\tilde{T}_{film}(\omega)}{\left(n_A + \tilde{p}^2n_B\right)Z_0\tilde{T}_{film}(\omega)} \quad (3)$$

where $\tilde{p} = \exp(-i\omega d_{sub}n_{sub}/c)$ represents the propagation term in a substrate with thickness d_{sub} [11].

Recently, it has been shown that it is also possible to perform reference-free extraction of dielectric and

electrical properties of substrates and thin conducting films from THz-TDS measurements [28, 29]. This is achieved by comparing individual transients from only the sample waveform, which means that the reference measurement can be omitted and furthermore decreases errors from signal fluctuations originating from the measurement setup such as timing jitter [26], periodic sampling errors [30], and uneven stage movement. From the directly transmitted pulse and the first internal reflection, $\tilde{\sigma}_s^{(\text{ref-free})}(\omega)$ is determined from $\tilde{T}_{\text{film}}^{(\text{ref-free})}(\omega) = \tilde{E}_{\text{film}}^{(1\text{st})}(\omega) \Big/ \tilde{E}_{\text{film}}^{(\text{dir})}(\omega)$ as [29]

$$\tilde{\sigma}_s^{(\text{ref-free})}(\omega) = \frac{n_B^2 \Delta\tilde{p} - n_A^2 \tilde{T}_{\text{film}}^{(\text{ref-free})}(\omega)}{Z_0 \left(n_A \tilde{T}_{\text{film}}^{(\text{ref-free})}(\omega) + n_B \Delta\tilde{p} \right)}, \quad (4)$$

where $\Delta\tilde{p} = \exp(-2i\omega d_{\text{sub}} n_{\text{sub}}/c)\exp(-i\emptyset_G)\exp(d_{\text{sub}}\alpha)$. Compared to $\tilde{p}$ in equation (3), the second term $\exp(-i\emptyset_G)$ is a correction for the Gouy phase shift $\emptyset_G$ [31], and the last term $\exp(d_{\text{sub}}\alpha)$ is an amplitude correction based on the absorption coefficient α of the substrate. These two additional terms are not necessary in equation (3) since they are equal for $\tilde{E}_{\text{film}}(\omega)$ and $\tilde{E}_{\text{sub}}(\omega)$ and cancel out. It is possible to determine d_{sub} from the distance between peaks in frequency domain from the Fourier transform of the full THz waveform including all transients. In practice, the correction terms for the amplitude and Gouy phase shift can be determined from one single calibration-like measurement [29]. This is advantageous compared to the standard referenced analysis in equations (1)–(3), where reference measurements must be acquired frequently to minimize effects from environment, mechanical stage movement and THz source fluctuations, all of which have no influence on the reference-free analysis. Also, at lower frequencies, where commercial spectrometers are operating, it is possible to extract meaningful electrical parameters for graphene on non-absorbing substrates without having to correct for amplitude and Gouy phase shift [29].

2.2. Conductivity analysis of THz-TDS spectra

The optical conductivity of graphene in the THz frequency range is mainly determined by intraband carrier transitions and the measured frequency-dependent sheet conductivity of graphene is well described by the Drude model [2–4, 6, 7, 14, 32, 33]

$$\tilde{\sigma}_s(\omega) = \frac{\sigma_{DC}}{1 - i\omega\tau}, \quad (5)$$

where $\sigma_{DC} = 1/\rho_s$ is the conductivity at $\omega = 0$. Figure 2(a) shows an example for graphene on SiC [9, 34] where $\tilde{\sigma}_s^{\text{dir}}(\omega)$ is fitted with the Drude model to obtain σ_{DC} and τ. From semiclassical Boltzmann transport theory [14, 35] the calculation of n and μ from σ_{DC} and τ follows as [6, 9, 12]

$$n = \frac{\pi\hbar^2}{e^4 \nu_F^2} \left(\frac{\sigma_{DC}}{\tau} \right)^2, \quad (6)$$

$$\mu = \frac{e^3 \nu_F^2}{\pi\hbar^2} \frac{\tau^2}{\sigma_{DC}}, \quad (7)$$

where ν_F is the Fermi velocity. While ν_F is often taken as a constant, it is necessary to renormalize ν_F (ν_F^*) due to interacting electrons in graphene [36–39], which are greatly affected by the dielectric environment, and thus the substrate. The square dependence of n, μ on ν_F in equations (6) and (7) highlights the importance of using the correct value for this parameter. The renormalization of ν_F is carried out for THz-TDS measurements of graphene [12], by determining ν_F^* as [39]

$$\frac{\nu_F^*}{\nu_F} = 1 + C(\alpha)\alpha \ln(\Lambda/k_F) \quad (8)$$

where $\Lambda = 1.75$ Å^{-1}, $k_F = \sqrt{\pi n}$, $C(\alpha) = (4(1+(\pi/2)\alpha))^{-1}$ and $\alpha = e^2/(4\pi\hbar\nu_F\varepsilon\varepsilon_0)$ [39]. We use $\nu_F = 0.85 \times 10^6$ m s^{-1} [36] and determine the effective permittivity ε as $\varepsilon = (\varepsilon_s + 1)/2$ using relative permittivity $\varepsilon_s = 4.4$ for SiO_2 substrate [40]. In practice, n, μ, ν_F^* are determined by iteratively solving equations (6) and (8) for n and ν_F^* and finally calculating μ from equation (7) based on the obtained value for ν_F^*.

The electrical parameters can also be extracted from reflection mode THz-TDS measurements [41] and a comparison between the conductivity extracted from transmission and reflection mode THz-TDS has also shown to yield similar results [42]. Reflection mode THz-TDS measurements of graphene will not be described in further detail here but have been described elsewhere [14, 41–44].

Complementary measurements have been performed in many cases in order to validate the extracted electrical properties of graphene measured by THz-TDS [14]. The measurements conducted for comparison with THz-TDS varies across a range of characterization methods including optical microscopy [29, 45], Hall measurements [6, 9, 12, 46], Raman spectroscopy [5, 8, 41], Kelvin probe force microscopy [8, 47], and micro four-point probe (M4PP) measurements [5, 8, 33, 48]. M4PP is a unique metrology technology developed by DTU and Capres A/S where the conductance is measured across a conducting wafer or thin film, using a 12-point microfabricated probe, with a probe pitch down to 1 μm [5, 14, 33, 49–52]. By combining the information from multiplexed four-terminal measurements (using different combinations of the 12 individual cantilever probes) according to specific protocols [48], values for the electrical properties can be extracted with far higher accuracy than ordinary M4PP measurements.

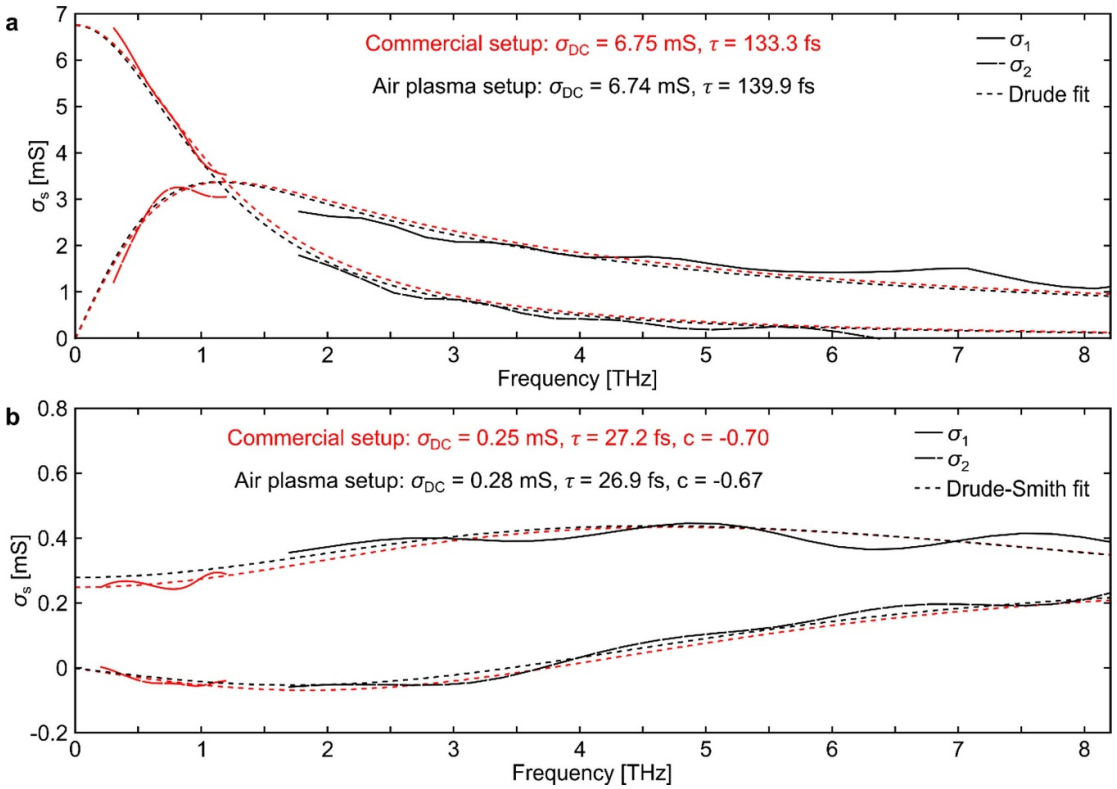


Figure 2. Comparison of THz-TDS frequency-dependent conductivity measured with commercial and air plasma setup. (a) Graphene on SiC fitted with the Drude model. (b) Graphene grown on Ge and transferred to HR-Si fitted with the Drude–Smith model.

2.2.1. Non-uniform graphene

In some instances, $\tilde{\sigma}_s(\omega)$ does not appear to follow the Drude model but instead at low frequencies shows a reduction in the real part of the conductivity while the imaginary part of the conductivity becomes negative as seen in figure 2(b). Such conductivity behavior has previously been reported for semiconductor nanostructures and thin metallic films at the metal–insulator percolation threshold [15, 53–57], and is characteristic of systems where the charge carriers experience some degree of preferential backscattering in addition to the isotropic scattering assumed in the Drude model. As the distance between line defects approaches the mean free path (average distance a charge carrier can travel until its initial velocity is randomized by scattering processes), the complex conductivity becomes increasingly difficult to describe with the Drude model.

For 2D materials, such behavior can originate from any line-shaped defect, including damage occurring in the transfer process (tears, rips, folds, wrinkles), lithographically defined edges (i.e. in arrays or gratings) but most commonly from grain boundaries that are present in nearly all graphene grown by chemical vapor deposition, as well as by most other synthesis methods [58]. Grain boundaries occur as crystal domains from multiple nucleation points coalesce to form a continuous film. At the grain boundary itself, the stitching of neighboring, rotated domains is typically facilitated by introduction of a line of 5–7 defects, which are more densely spaced for large grain misalignment angles [59]. Moreover, the momentum mismatch between misaligned neighboring grains contributes to the energy barrier that leads to reflection and carrier localization.

The conductivity response has in these cases been described by the phenomenological Drude–Smith model developed for systems with some degree of carrier localization [60, 61]. The Drude–Smith model is expressed to first order as [60]

$$\tilde{\sigma}_s(\omega) = \frac{W_D}{1 - i\omega\tau}\left(1 + \frac{c}{1 - i\omega\tau}\right), \qquad (9)$$

where W_D is the Drude weight ($\sigma_{DC} = W_D(1 + c)$) and the parameter c ($-1 \leqslant c \leqslant 0$) describes the degree of preferential backscattering. If $c = 0$, the ensemble carrier momentum is relaxing exponentially on a timescale of τ, which in the Drude model is also the carrier scattering time. In the Drude model, every scattering event randomizes the momentum. In contrast, during THz measurements all carriers are backscattered during one cycle of the AC-field for $c = -1$ (complete suppression of DC conductivity). The Drude–Smith model has previously been applied to graphene in cases where the homogeneity of the graphene layer was suspected to be low [33, 62] and also provides a good fit to $\tilde{\sigma}_s(\omega)$ in figure 2(b) for

graphene grown on Ge [63, 64] and transferred to HR-Si [65]. We note that due to the phenomenological nature of the Drude–Smith model, it is not clear how the extracted scattering time should be interpreted, whether macroscopic carrier mobility can be extracted and what exactly the physical meaning of a non-zero backscatter parameter means. Alternative interpretations of the Drude–Smith model as well as alternative models are therefore being developed and discussed in literature [15, 66–70].

Figure 2 shows Drude and Drude–Smith model fits to measurements carried out with the commercial as well as the air plasma setup, see section 2.1. With its much broader frequency range the air plasma setup allows us to extend and verify the values extracted for σ_{DC}, τ, and c with the commercial setup, due to the greater accuracy of the fits to the broader spectrum. As seen in figure 2 we obtain similar values from both setups, which has also been shown for different cases of graphene on HR-Si [33] and PET [12].

Both the Drude and Drude–Smith behavior is successfully described using classical Monte Carlo simulations [69]. Here the motion of carriers subject to isotropic (Drude) and boundary scattering (preferential backscattering) is calculated to generate conductivity spectra that can be directly compared to conductivity spectra extracted from THz-TDS measurements. We employ a strategy inspired by the impulse response approach [69] where an ensemble of carriers (travelling at a constant Fermi velocity v_F) are designated an initial finite average momentum, corresponding to a drift velocity obtained for a constant electrical field and a certain carrier mobility. In the absence of the electrical field, scattering on isotropically scattering defects corresponding to a certain mean free path ℓ_{mfp} and carrier mobility μ as well as scattering on boundaries (with reflection coefficient, $0 < R \leq 1$) causes the average current to decrease towards zero over time. The frequency-dependent conductivity is obtained by Fourier-transforming the time-dependent current $I(t)$ extracted from averaging over 10^5–10^6 trajectories. In figure 3 we show the simulated conductivity spectra for graphene with a carrier mobility of 2150 $cm^2\ V\ s^{-1}$ and a carrier density of $10^{12}\ cm^{-2}$, which are typical numbers for CVD graphene on a SiO_2 substrate. The resulting mean free path $\ell_{mfp} =$ 25 nm, can be found from the Boltzmann transport equation $\sigma_{DC} = (2e^2/h)k_F\ell_{mfp}$ and $\sigma_{DC} = ne\mu$. A network of partially ($0 < R < 1$, figure 3(a)) or fully reflecting ($R = 1$, figure 3(b)) boundaries mimics a grain boundary landscape with average grain sizes of 125 nm, 250 nm, 500 nm and up to 4000 nm, which can be compared to the boundary-free Drude conductivity (black lines). For $R = 1$ (figure 3(b)), domain sizes up to 4 μm exhibit the depression of the DC conductivity characteristic of preferential backscattering, despite the grain size being 160 times larger than the mean free path. This shows that carrier localization effects can be present for much lower line defect densities (or grain sizes in the case of polycrystalline graphene) than anticipated in our previous work [33], indicating that THz-TDS may be helpful in analyzing the microstructure of graphene films. More work needs to be done, however, to accurately determine the device carrier mobility for small-grain graphene films with strong non-Drude-like behavior, which may be particular prevalent for direct CVD growth on substrates like SiC [7, 8], SiO_2 and sapphire[1] where grain sizes are typically smaller than on copper substrates, as well as high-throughput R2R CVD reactors.

3. Case studies

In the following we present different case studies of THz-TDS measurements of graphene. First, we show that values for σ_{DC} extracted from the Drude–Smith model agree well with reference measurement across 4 inch silicon wafer substrates covered with graphene. The remaining cases includes a highlight of recent developments in reference-free analysis and examples showing the relevance of THz-TDS in various graphene production and optimization scenarios.

3.1. Graphene conductivity from the Drude–Smith model

Values of σ_{DC} extracted from THz-TDS conductivity spectra following the Drude model have been validated several times against Hall and M4PP measurements [6, 8, 11, 33, 47]. There is however comparatively limited data available [62, 71] for measurements of graphene when $\tilde{\sigma}_s(\omega)$ does not appear to follow the Drude model and in particular for measurements at 4 inch wafer-scale.

A map of σ_{DC} extracted from the Drude–Smith model for a 4 inch wafer covered with graphene (from Graphenea, Spain) measured by THz-TDS is shown in figure 4(a). The sample shows a base conductivity of ~2 mS with clearly defined lines of lower conductivity. The origin of these lines is not clear. A high-resolution optical map of the sample does not reveal any distinct non-uniformities, such as tears and scratches in the graphene layer. Figure 4 shows values of c and σ_{DC} from THz-TDS together with the sheet conductance (G_s) from M4PP following a line scan across the wafer with 1 mm step size. The M4PP measurements were performed with 10 μm probe pitch on a CAPRES microRSP-A300 measurement system using a newly developed sub-probe analysis for conductivity retrieval [48]. The values of σ_{DC} and G_s are in reasonable agreement, and show similar, distinct variations at positions matching the low conductivity lines in the wafer map. This indicates that THz-TDS can be used for large-area conductivity maps, even when the individual conductivity

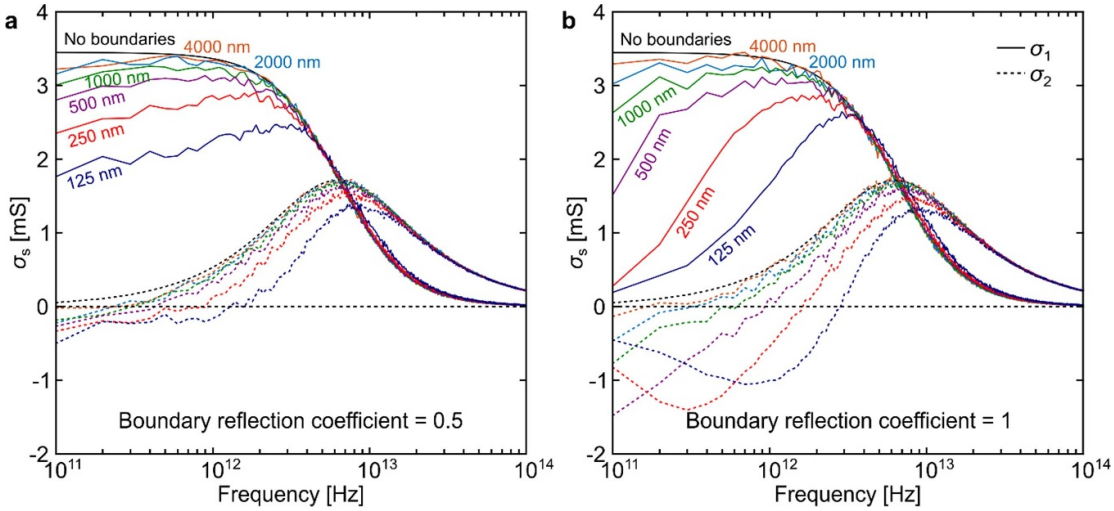


Figure 3. Monte Carlo simulated conductivity spectra for graphene with average grain boundary size from 125 nm and up to 4000 nm and a mean free path of 25 nm, for boundary reflection coefficient (a) $R = 0.5$, (a) $R = 1$. Full lines indicate the real part σ_1 and dashed lines indicate the imaginary part σ_2 of the complex sheet conductivity σ_s.

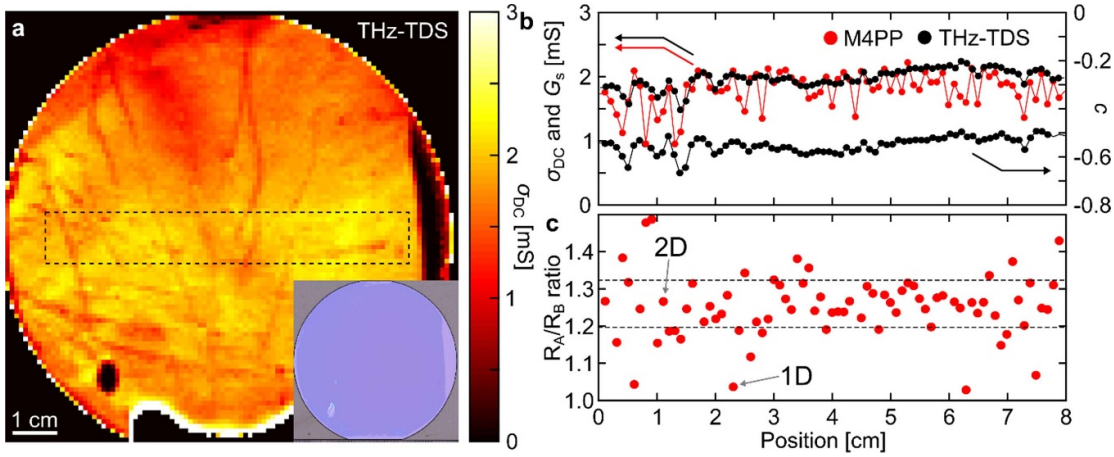


Figure 4. (a) THz-TDS map of σ_{DC} for graphene transferred to an oxidized 4 inch HR-Si wafer. Inset shows optical map of the sample generated by stitching together multiple, high-resolution optical images. (b) Line plot of σ_{DC} taken inside the rectangle in (a) together with M4PP G_s values from a scan along the same line. The THz-TDS Drude–Smith c parameter along the same line is also shown on the opposite y-axis. (c) Line plot of the R_A/R_B resistance ratio for the M4PP line scan shown in (b). The dashed lines indicate ±5% deviation from a R_A/R_B resistance ratio of 1.26.

spectra are non Drude-like. The dips in conductivity are clearly more substantial for the M4PP measurement compared to THz-TDS. This discrepancy stems from an important difference between the two methods that becomes particularly apparent for non-continuous samples, i.e. with line-defects and tears. An electrical measurement, even with such small probe spacing as the M4PP (10 μm), can be completely disrupted by a line defect between the source and drain. The THz-TDS measurement, however, measures an average (over the THz spot size of ~400 μm) of the local conductivity in every spot of the graphene film, irrespective of whether the current can flow across a line defect or not. The characteristic length scale of this 'locality' is roughly given by the diffusion length, which is typically less than 100 nm [14]. It is also seen in figure 4(b) that c and σ_{DC} are seen to be correlated, implying that preferential backscattering has a detrimental impact on DC conductivity.

By performing M4PP measurements in two configurations (A, B) it is possible to determine whether the current flow in the sample is qualitatively one- or two-dimensional (1D or 2D) from the R_A/R_B resistance ratio, where A and B correspond to two complementary current–voltage configurations, i.e. A($I_{1,4}$, $V_{2,3}$) and B($I_{1,3}$, $V_{2,4}$), following the notation described in detail elsewhere [14]. If $R_A/R_B = 1$ the current flow is said to be 1D-like, while a uniform conductor will exhibit $R_A/R_B \approx 1.26$ [72–74]. Figure 4(c) shows a line plot of the R_A/R_B resistance ratio across the same line as in figure 4(b). Interestingly, the M4PP R_A/R_B resistance ratio shows that the current flow is overall 2D-like

despite the Drude–Smith backscattering parameter c of around -0.55, which indicates that there is a reasonable degree of carrier localization. This highlights that further work towards understanding of the exact physical interpretation of non-Drude-like conductivity spectra in THz-TDS for graphene is necessary.

3.2. Reference-free analysis

For THz-TDS measurements of samples where the individual transients from the directly transmitted pulse and the internal reflections are well-separated in time (see figure 1(d)) it is possible to extract $\tilde{\sigma}_s(\omega)$ without performing the standard reference scan [29]. This is desirable for substrates that are fully covered by graphene where the reference measurement has to be performed on a different sample and in production scenarios where a THz-TDS system will be running for extended periods with possible fluctuations from THz source, environment, and mechanical movement being very likely.

An optical map and the corresponding graphene coverage map of a sample is shown in figures 5(a) and (b). The graphene coverage map was generated by comparing the red, green, and blue contrast from each recorded pixel of the optical map to the theoretically calculated contrast for single layer graphene (SLG) and bilayer graphene on 90 nm SiO_2 substrate [75]. The graphene is homogeneously single layer and covers the sample continuously, except from some small holes at the center left. A higher magnification image (figure 5(c)) also confirms that the graphene is continuous on a smaller scale. Conductivity maps obtained from standard referenced analysis (equation (2)) and reference-free analysis (equation (4)) are shown in figures 5(d) and (e) and look very similar. Both are obtained by fitting each spatial point measurement with the Drude model. The conductivity looks homogeneous at ∼2.5 mS for both maps with a small region of lower conductivity at the center left, where the optical images show a small hole. The histograms for σ_{DC}, τ, n, and μ in figures 5(f)–(i) show very similar distributions, where the median values vary very little (<5%), which is also the case for ν_F^* as shown previously [29] and shows that the method is certainly applicable. The data shown here for reference-free analysis includes a Gouy phase shift correction, while the amplitude correction is not necessary for HR-Si with negligible absorption [76] at low THz frequencies. Similar results for median values are obtained by using the reference-free analysis without Gouy phase shift correction, which, however, results in a larger spread in the histograms.

The graphene sample used for reference-free analysis was grown to ensure a Drude like frequency-dependent conductivity. Adlayers and grain boundaries, as discussed in section 2.2, can degrade the performance of graphene, and result in inhomogeneous performances from device to device [58, 77, 78]. The grain boundaries occur when graphene grains of different crystallographic orientations join together during CVD growth of large area graphene on metallic (normally Cu) surfaces [58, 79], while adlayers (bilayer or multilayer regions nucleated from the subsurface carbon in a Cu substrate) are almost always present in CVD grown graphene films [77].

Epitaxial growth of graphene on a single crystal substrate (e.g. Cu(111), Cu/Ni(111) alloy surface) with a lattice spacing closely matched to graphene is promising to achieve single crystal graphene film over a large area. Aligned graphene islands have been reported to grow on the surface of single crystal Cu(111) and Cu/Ni(111) alloy and to merge without the presence of grain boundaries in the joining regions [77, 80–84]. Note that commercial polycrystalline metal foils can be reproducibly converted to single crystal Cu(111) (and other metal foils including Ni(111), Pt(111), and Co(0001)) using a contact-free annealing method under Ar and H_2, while single crystal Cu/Ni(111) alloy foils with fine tuning of the Ni concentrations can be generated by electroplating various amounts of Ni on both sides of the produced Cu(111) foil followed by an extra annealing [80, 85, 86]. Annealing in hydrogen gas atmosphere is found to deplete any subsurface carbon in a Cu foil, thus adlayer-free single crystal graphene film can be grown on Cu(111) foils made by contact-free annealing [86]. The single crystal graphene film used here contains parallel, centimeter-long, ∼100 nm wide folds (formed due to the thermal contraction of the Cu(111) foil during cooling) separated by 20–50 μm. Though the carrier mobility of a graphene field-effect transistor is significantly decreased if the active region contains fold(s), the highly-oriented folds allow straightforward fabrication of devices in the regions between adjacent folds, because these regions are homogeneously single layer and single crystal [77]. The single crystal nature of the graphene film and the lack of adlayers limits the number of defects and grain boundaries that typically lead to Drude–Smith like features in the conductivity spectrum.

3.3. Encapsulated graphene

In order to achieve consistent, high quality electronic performance of graphene devices it is necessary to encapsulate them to shield the graphene layer from the surrounding environment due to adsorbates [87, 88]. This encapsulation of graphene can be achieved by the use of dielectric 2D materials such as hexagonal boron nitride (hBN) [89] or atomic layer deposition (ALD) of dielectrics such as Al_2O_3 [90–92]. However, once graphene samples are encapsulated it is difficult to measure the electrical properties without specialized contact

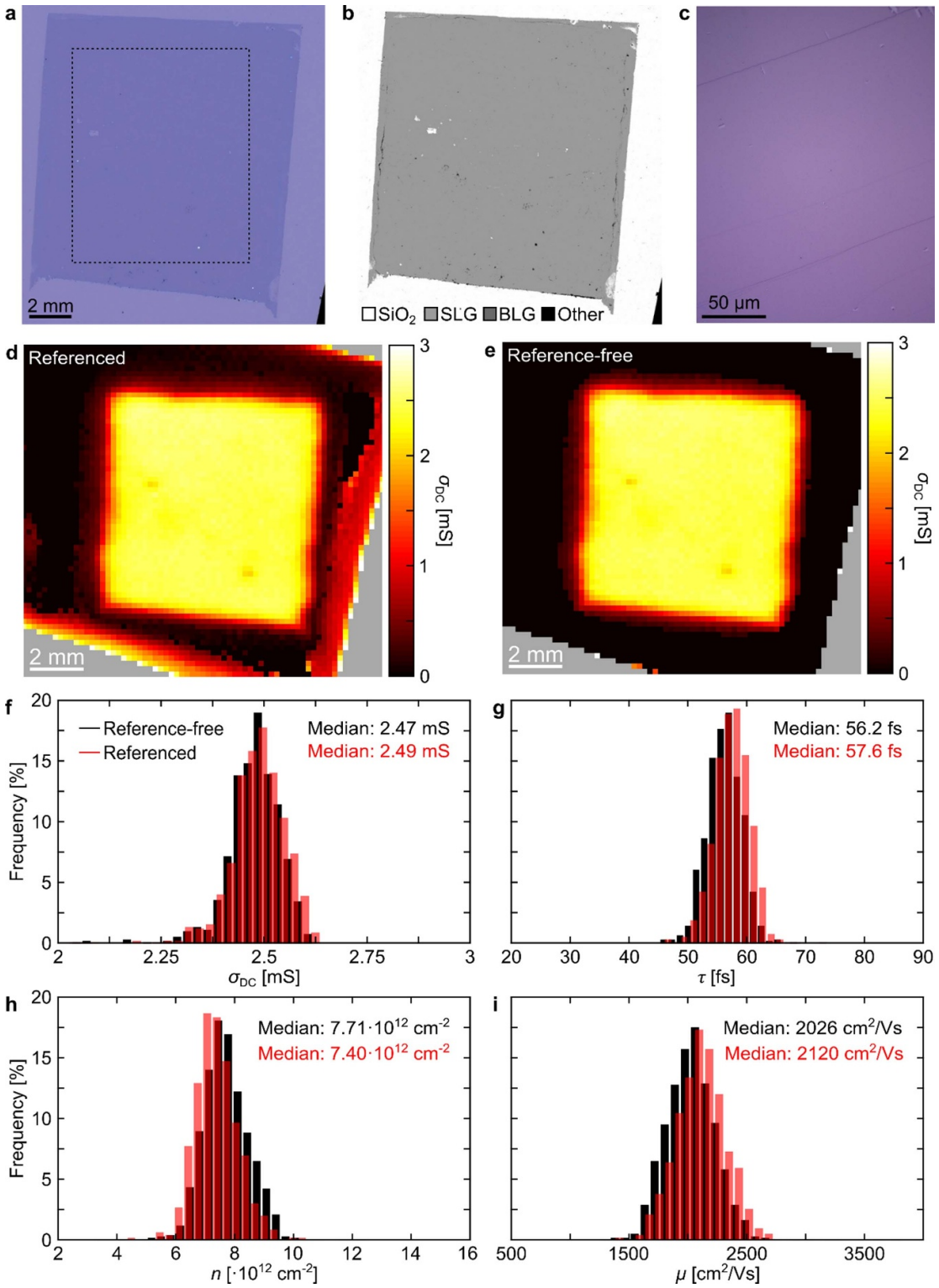


Figure 5. (a) Optical map of graphene on 90 nm SiO_2/Si substrate. (b) Graphene coverage map of the sample shown in (a). (c) High magnification image from sample shown in (a). (d), (e) THz-TDS σ_{DC} maps of graphene sample shown in (a) based on (d) standard referenced analysis and (e) reference-free analysis. (f)–(i) Histograms with comparisons of electrical parameters extracted from reference-free and standard referenced analysis. (f) σ_{DC}. (g) τ. (h) n. (i) μ. Values for histograms are from within dotted square in (a).

designs and following complex sample fabrication [93]. This is inconvenient and expensive for the finished encapsulated material and following the impact of intermediate process steps on the electronic performance becomes nearly impossible.

Since the dielectric materials used for encapsulation are generally transparent to THz radiation, THz-TDS can be used to assess the electrical properties of encapsulated graphene, as well as after each of the process steps leading to the final

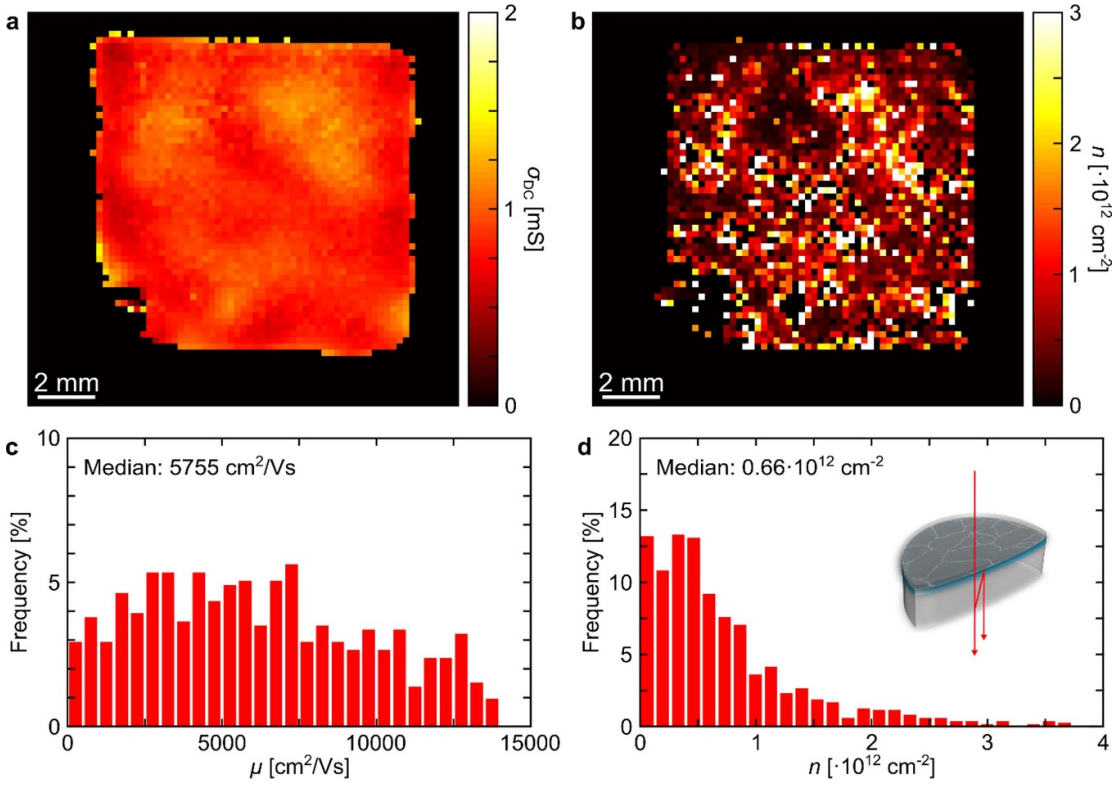


Figure 6. THz-TDS measurement of ALD encapsulated graphene. (a), (b) Maps of σ_{DC} and n. (c), (d) Histograms of μ and n.

results, simply because it is non-destructive and non-invasive. This has already been done for hBN encapsulation, where THz-TDS and Hall device measurements gave very similar results [46].

Here we show that the electrical properties can also be determined for graphene encapsulated by 30 nm ALD Al_2O_3 using a process described in detail by Mzali *et al* [92]. Since the 10 × 10 mm^2 sample is fully covered by encapsulated graphene, we use the reference-free analysis (equation (4)) without corrections to extract the electrical properties from the THz-TDS measurement with all spectra fitted with the Drude model. Figure 6(a) shows a map of σ_{DC} for the sample. The conductivity is split into areas of higher and lower conductivity, which is even more distinct in the map of n (figure 6(b)). From the THz-TDS measurement itself it is not possible to determine whether this originates from the graphene growth or transfer process. Although the spread is relatively larger, the histograms of μ and n in figures 6(c) and (d) shows values that compare well to results from similarly fabricated graphene field effect transistors (FETs) [92], where mobility values of ∼6000 cm^2 V s^{-1} are reported. An even better match appears for the distribution of n, which is very similar to the FET results [92], with a majority of the distribution <0.5 × 10^{12} cm^{-2} and a steady decrease that ends at 4 × 10^{12} cm^{-2}.

3.4. THz-TDS for graphene quality control

THz-TDS has so far mainly been used for graphene characterization after transfer due to growth most commonly being carried out on metallic surfaces, in particular Cu. However, the clear advantage of direct growth on dielectrics, emphasizes the importance of being able to carry out characterization on as-grown graphene on such substrates. Here we show examples of how THz-TDS can be employed for quality control and process optimization in different steps of the fabrication cycle of graphene.

3.4.1. Growth optimization

SiC was one of the first THz transparent substrates that graphene growth was conducted directly onto [34, 94]. Graphene has since also been grown on SiN [95], glass [96, 97], and sapphire [10]. In figure 7 we show examples of THz-TDS mapping of as-grown graphene on 4 inch sapphire wafers [10], which were produced using different graphene growth conditions. The result seen in figure 7(a) is symptomatic of a deposition onto a bowed wafer at high temperature; this can be resolved by precise control of the temperature ramping and heat distribution over the wafer. The sample in figure 7(b) has incomplete graphene growth, which is resolved by optimizing the carbon source flow and exposure time. The conductivity maps in figures 7(a) and (b) obtained from fitting with the Drude–Smith model show clear inhomogeneity in σ_{DC} across the wafer, while the conductivity achieved is much more homogeneous in figure 7(c) after tuning the process conditions. This is clearly seen in the histogram in figure 7(d), where the standard deviation drops from 21.4% and

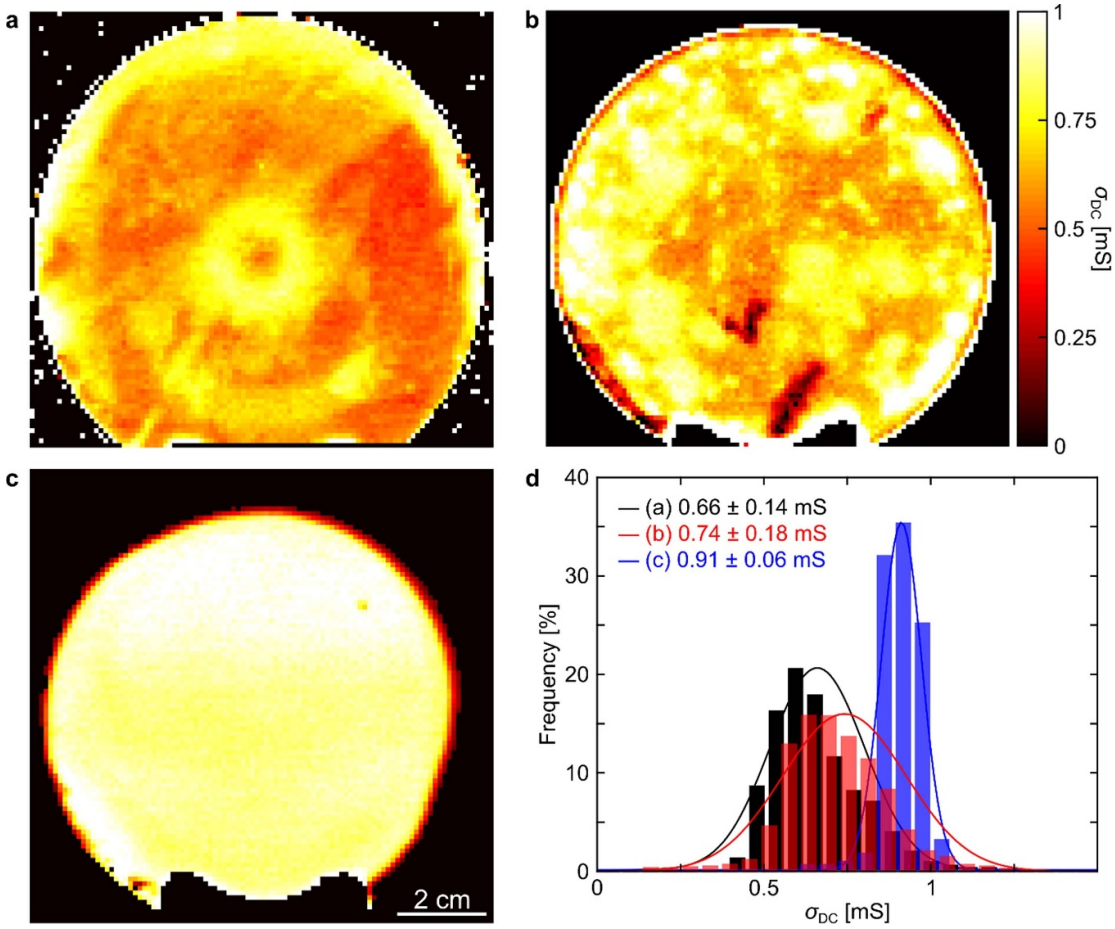


Figure 7. (a)–(c) THz-TDS conductivity maps of graphene as-grown on sapphire substrates using different growth conditions. (d) Histogram of σ_{DC} for the maps in (a)–(c). The scale bar and colorbar is the same for (a)–(c). (c) Adapted from [10].

24.9% in (a) and (b) to only 6.6% for (c). By wafer-scale mapping of the electrical properties of as-grown samples before any transfer processing it becomes significantly easier to perform direct optimization of the graphene growth process without having to disentangle whether defects measured post-transfer are growth-related or transfer-related.

3.4.2. Transfer optimization

Intercalation of water between graphene and the growth substrate has led to an advancement in transfer methods that are non-destructive towards the graphene growth substrate [98–101]. Here we use THz-TDS to measure the conductivity of graphene grown on sapphire [10] before and after attempted water intercalation in order to investigate the effects of a similar process for this system. Figures 8(a) and (b) shows THz-TDS conductivity maps of graphene on sapphire before and after attempted water-intercalation (de-ionized water, 50 °C, 24 h). The 24 h submersion in water seemed to have little effect on the measured conductivity as also seen in figure 8(c), where the average conductivity for both maps is within the standard deviation from a fit of each histogram to a normal distribution.

Although there does not seem to be a measurable effect of the water submersion on the THz-TDS results, we still find that the method gives useful information when performing a peeling-based transfer using poly(vinyl alcohol) (PVA) as the transfer polymer [101]. Figures 8(d) and (e) shows THz-TDS conductivity maps of a sample of as-grown graphene on sapphire and the same graphene layer after PVA-based transfer to an oxidized HR-Si substrate. The sample seems to contain more holes after transfer as also observed in the graphene coverage map (figure 8(f)) and the conductivity is clearly lower after transfer compared to as-grown on sapphire (figure 8(g)). Just as THz-TDS can benefit growth characterization (section 3.4.1) it can also be used to determine whether defects in transferred graphene origin from the growth process or from the transfer process, and thereby aid in disentangling otherwise complex process diagnostics. Although the lower graphene conductivity after transfer may be due to the additional holes and defects in the graphene layer we cannot completely rule out that a difference in the coupling between graphene and substrate (sapphire vs SiO_2) also has a role to play.

An example of how THz-TDS can be used to spot inhomogeneities in graphene on oxidized HR-Si

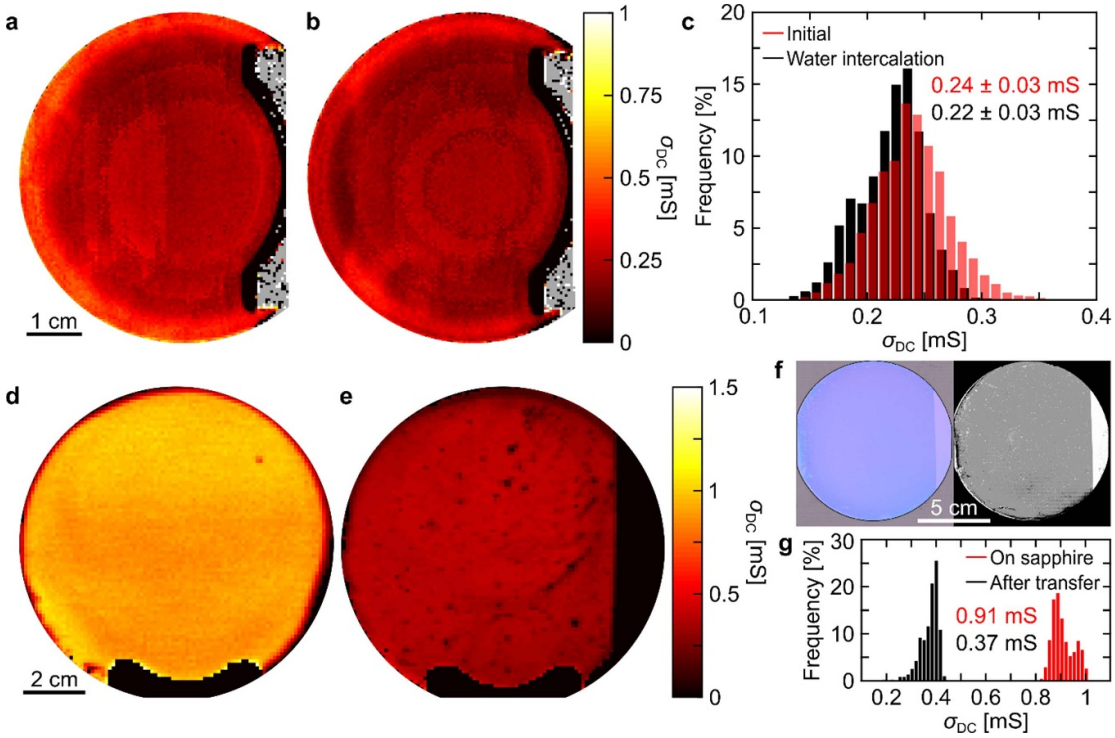


Figure 8. (a), (b) THz-TDS conductivity maps of graphene on 2 inch sapphire wafer (a) as-grown and (b) after attempted wafer-intercalation. (c) Histogram of σ_{DC} for the central region of the maps in (a), (b). (d), (e) THz-TDS conductivity maps of graphene (d) as-grown on 4 inch sapphire wafer and (e) after transfer to oxidized HR-Si substrate. (f) Optical and graphene coverage maps of the sample in (e). (g) Histogram of σ_{DC} for the central region of the maps in (d), (e). Panels (d), (f) and (g) are reprinted with permission from [10] Wiley.

that appears homogeneous from optical microscopy is shown in figures 9(a) and (b) that shows an optical and THz-TDS conductivity map of the same sample. From the optical map the sample appears homogeneous, except from a hole near the upper right corner. That hole is also visible in the THz-TDS conductivity map, which also highlights several additional features in the sample. The conductivity does not appear homogeneous but varies in a patchwork style. The sample was further measured by Raman spectroscopy to verify whether the conductivity variation measured by THz-TDS was real. Figure 9(c) shows a map of the Raman G peak position, which has been correlated to the doping level of the graphene layer [102, 103]. The map of the Raman G peak exhibits the same features as the THz-TDS conductivity map and confirms that the pattern observed in the conductivity is in fact real and not a measurement artefact.

We speculate that the peculiar pattern in the conductivity shown in figure 9(b) is caused by inhomogeneous application of pressure in a stamping system for graphene transfers. The correlation between the THz-TDS conductivity and Raman G peak has also been discussed previously [41], and THz-TDS has earlier proven to be able to highlight defects in graphene on PET not visible to the eye, or even with optical microscopy [11].

3.4.3. Post-transfer optimization

THz-TDS can be used to measure the electrical properties of encapsulated graphene as shown in section 3.3 for ALD Al_2O_3 passivated graphene. This demonstrates that THz-TDS can be used to optimize such layers by performing fast, non-destructive measurements of the electrical properties between process steps. Al_2O_3 encapsulation of graphene can be performed in a two-step process (figure 10(a)), where a thin (1 nm) AlO_x protection layer is first deposited by electron beam evaporation followed by an ALD Al_2O_3 passivation layer [92]. Here we perform several THz-TDS measurements of four samples to reveal the influence of each process step; first we measured the bare graphene layer, then we measured again after AlO_x protection was added, and finally after full ALD Al_2O_3 passivation. The measurement time per sample was <10 min for each step.

Figures 10(b)–(f) show bar plots of the evolution in σ_{DC}, τ, n, μ, and ν_F^* for each process step for the four samples. There was no ALD Al_2O_3 passivation layer added for sample 1 for reference purposes. While the initial conductivity is relatively similar for all four samples (within ~5%), there is more variation for τ, n, and μ. The general trends are decrease and stabilization of σ_{DC} after AlO_x protection, with little further decrease after ALD Al_2O_3 passivation. After both process steps τ and μ increases

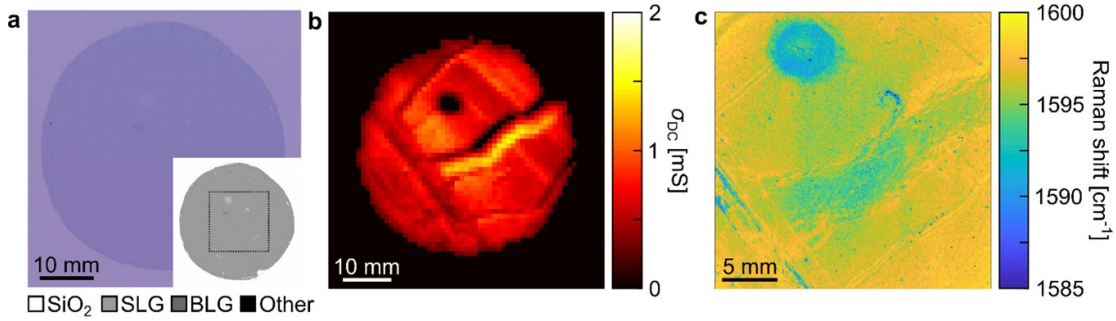


Figure 9. (a) Optical map of 2 inch graphene area transferred from Cu growth substrate to oxidized HR-Si. Inset shows the corresponding graphene coverage map. (b) THz-TDS map of σ_{DC} for the sample in (a). (c) Map of the Raman G-peak position from the region highlighted by dotted square in the graphene coverage map in (a).

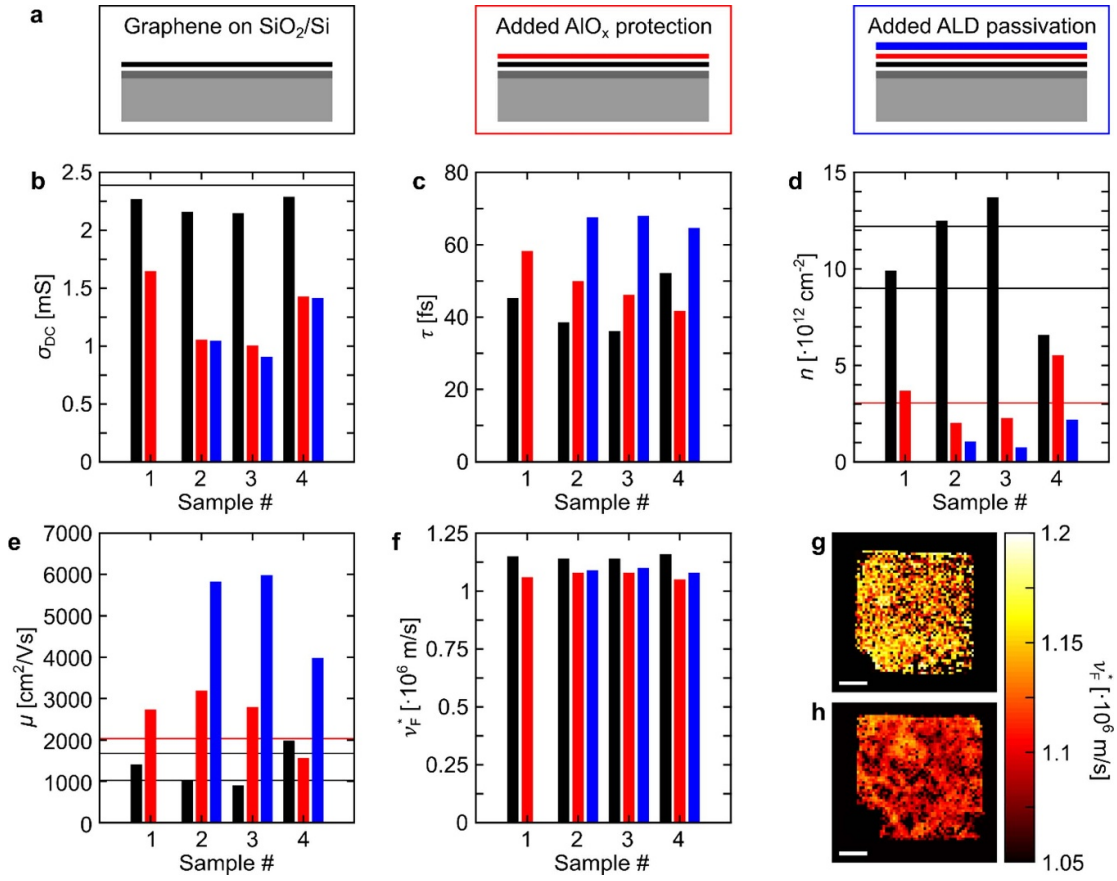


Figure 10. (a) Illustration of process flows for passivation of graphene, showing a sample without passivation (black box), with AlO_x protection (red box), and with protection and ALD Al_2O_3 passivation (blue box). (b)–(f) Bar plots of the evolution in electrical properties (median value for σ_{DC}, τ, n, μ, ν_F^*) of graphene for each process step for four different samples. The process step is indicated by the color of the bars, which correspond to the color of the boxes in panel (a). Horizontal lines in (b), (d), (e) indicate values measured by complementary technique on the same samples with process step indicated by color of the line. (g), (h) THz-TDS maps of ν_F^* for sample 3 (g) without passivation and (h) after protection and passivation processes.

while n decreases. For ν_F^* there is a decrease after AlO_x protection and a small increase after ALD Al_2O_3 passivation as also seen in the ν_F^* maps in figures 10(g) and (h). The change in ν_F^* from bare to processed graphene is mainly driven by the fact that we use a value of 9.4 for the relative permittivity of the deposited aluminum oxide [104] instead of 1 for air in equation (8).

Several reference measurements were conducted on the same samples to validate the THz-TDS results and the change of relative permittivity for aluminum oxide. These measurements are indicated by horizontal lines in figures 10(b), (d) and (e). A sheet conductance of ~2.4 mS for initial samples was measured by a Lehighton LEI 1500E, which matches the THz-TDS σ_{DC} values within 10%. Hall

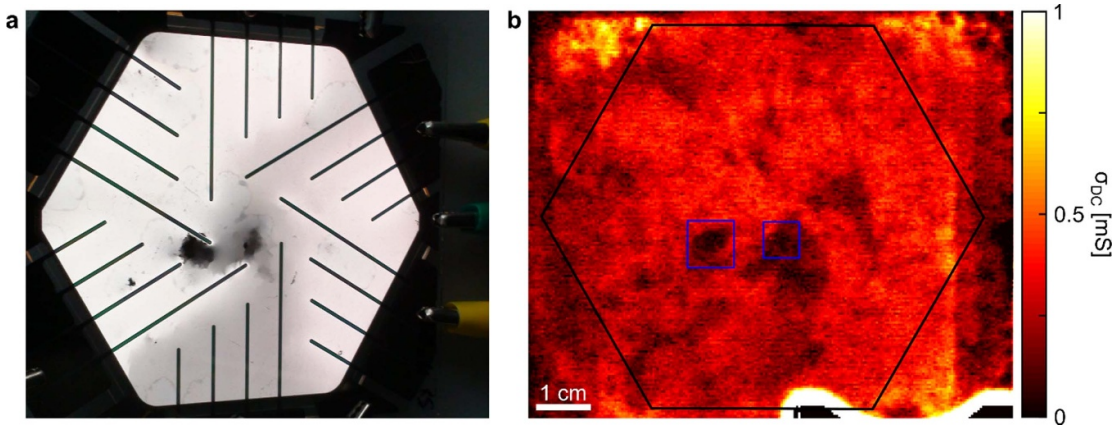


Figure 11. (a) Photograph of light emission from a white OLED with graphene as transparent electrode (anode). Image is courtesy of Fraunhofer FEP. (b) THz-TDS conductivity map of the graphene on quartz sample used for OLED in (a) before deposition of active layers and metallic back side contact. Blue squares in (b) highlight the position of the two clearly visible defects in the OLED in (a).

effect measurements of n_H and μ_H were conducted for samples before and after AlO_x protection, with reasonable agreement with the THz-TDS values. No measurements were performed on these samples after ALD Al_2O_3 passivation due to difficulties in fabrication of side contacts. However, for samples fabricated similarly to sample 3, it was previously shown [92] that n is generally below 3×10^{12} cm^{-2} after AlO_x protection and below 1×10^{12} cm^{-2} after ALD Al_2O_3 passivation, while μ can reach values of ~6000 cm^2 V s^{-1} after ALD Al_2O_3 passivation. These results all agree well with the THz-TDS values reported here.

We note that different deposition parameters and Al_2O_3 thicknesses (15–30 nm) were used for the four samples and the initial values for the electrical properties varied between samples, so exactly similar results for the four samples should not be expected—indeed, these results show how THz-TDS can be used for optimizing process parameters of the ALD process flow. THz-TDS could also work for layers buried deeper inside the substrate. This, however, would require changes to the transmission function model used for parameter extraction from the system.

Another example of the use of THz-TDS in quality control is for early diagnosis and testing prior to device finalization in relation to transparent electrode applications, where the graphene layer will usually be present on a transparent substrate. One example is organic light emitting diodes (OLEDs) where graphene can be transferred to a glass or polymeric substrate before deposition of active organic layers and a (often metallic) back side contact. THz-TDS can be used to screen the quality (conductivity, homogeneity) of the graphene layer before initiating further process steps. An example of how this can benefit is shown with a white graphene-based OLED in figure 11(a). The active area is 42.3 cm^2 and the OLED emits relatively uniformly, except from two clear defected areas close to the center of the sample. These two defects were also present in a THz-TDS conductivity map of the graphene on quartz substrate before OLED processing (figure 11(b)), while not visible to optical inspection. Previous results have also shown that THz-TDS is effective for measuring the effects of chemical post-transfer doping of graphene to increase the conductivity [14] and for comparing electrical properties of graphene before and after device fabrication [105, 106].

3.5. THz-TDS in production scenarios

In section 3.4 we showed several examples of how THz-TDS can be used to optimize both growth, transfer, and post-transfer processing of graphene. Since the production of graphene has matured to a point, where large samples of graphene on 12 inch Si [107] and 25 × 30 cm^2 PET [11] can be fabricated, we will discuss here how THz-TDS can be applied in real production scenarios in particular with respect to measurement speed and on relevant substrates.

3.5.1. THz-TDS scanning of 12 inch wafers in 1 h

One method of fabricating large areas of graphene is batch fabrication, where graphene is grown simultaneously on a batch of growth substrates and with individual transfers to a target substrate. Since silicon is a standard substrate for most electronic devices, we here discuss how to rapidly characterize graphene on 12 inch HR-Si wafers. The exact time for a measurement scan to be rapid can be discussed, but here we show that it is possible to measure the conductivity of graphene across a 12 inch HR-Si wafer with 1 mm step size within 1 h. Given the time and step size, this takes 0.04 s of measurement time per measurement point considering a square sample of 300 × 300 mm^2. The used commercial spectrometer (see section 2) acquires THz-TDS spectra at 100 Hz. It is therefore maximally possible to measure and average four waveforms per measurement point for a 1 h scan.

Such a scan was performed for the THz-TDS conductivity map shown in figure 12(a). It is noted that the 12 inch diameter HR-Si wafer is only covered by 4 inch diameter graphene placed centrally on the wafer due to fabrication constraints. However, the measurements were conducted in such a way that it would have taken exactly the same time and have the same precision if more or all of the wafer was covered by graphene as the full 12 inch wafer was mapped with the required scanning speed.

A reference measurement was performed in order to validate the THz-TDS conductivity map obtained from a 1 h scan of a 12 inch wafer. Several comparisons between σ_{DC} from THz-TDS and G_s from M4PP or Hall measurements have been made showing that THz-TDS works as an efficient probe of σ_{DC} for graphene [5, 6, 8, 9, 11, 14]. The THz-TDS performed for such comparisons average over 20–50 waveforms per measurement point. The reference measurement was following performed with acquisition of 50 waveforms per measurement point and took 12.5 h to complete. The THz-TDS conductivity map of the reference measurement is shown in figure 12(b). The 1 h scan and the 12.5 h scan are nearly identical, despite a small shift in average conductivity, which is easily within the typical variations due to random fluctuations in humidity and temperature [42, 88]. This is confirmed by the histogram of σ_{DC} from the two maps (figure 12(c)) that shows a slightly larger conductivity for the reference measurement. However, the deviation is only 4.1% when comparing average values from fitted normal distributions, which shows that is possible to perform trustworthy measurements of the conductivity of graphene with 1 mm step size across 12-inch wafers within 1 h.

We emphasize that the results for the 1 h scan of 12 inch wafers were obtained with a commercial setup that was introduced in 2007. Since then, progress in THz technology allows performance well beyond what is shown in figure 12, both in terms of speed and measurement accuracy. As an example, we show in figure 13 the frequency-dependent conductivity of graphene on SiC measured with the same setup used for figure 12 (and most other results presented in this work) compared to a Toptica TeraFlash Smart spectrometer based on electronically controlled optical sampling [108, 109]. We note that the THz-TDS measurements for figure 13 were conducted on three different samples and that a comparison of the Drude model fits is not the aim of the figure. The improved frequency bandwidth with the new system is clearly seen, which should provide improved accuracy when fitting data with the Drude model. Furthermore, the new spectrometer is capable of acquiring THz-TDS spectra at 1600 Hz — a 16× improvement compared to the setup used for figure 12. Considering the vast improvements in speed and spectral bandwidth offered by modern, yet affordable THz spectrometers in general we anticipate that 12 inch graphene wafer scans within 5–10 min is possible.

3.5.2. Graphene on polymers for R2R setups

R2R production of graphene is perhaps the most obvious method for large-area production, especially for graphene onto polymeric substrates, where graphene is grown on a rolling metallic foil and transferred onto a roll of polymeric material. Examples of graphene growth and transfer methods compatible with R2R production have been shown already [101, 110, 111]. There are at present no options for inline characterization of the electrical properties of graphene in a R2R production line, perhaps with the exception of THz-TDS. THz-TDS has proven to be capable of reliably measuring σ_{DC} of graphene on PET substrate across 25 × 30 cm^2 samples (figure 14(a)) [11] and recently values of n and μ measured for graphene on PET and polyethylene naphthalate (PEN) by THz-TDS were verified by reference measurements [12].

Figure 14(b) shows maps of n and μ for graphene across 25 × 30 cm^2 substrates with corresponding histograms in figures 14(c) and (d). The maps of n and μ appear homogeneous (standard deviation <10% of average) in half of the map (∼17 500 measurement points), but are inhomogeneous in the other half and that there is a clear vertical line pattern in the inhomogeneities. We ascribe these errors to drift in either the THz source or the mechanical stage and not the sample itself. This underpins a consideration that must be taken into account for R2R integration of THz-TDS systems. In this case the measurement artifacts could have been mitigated by using a THz-TDS system with short THz pulse duration making it possible to measure individual transients on thin polymer substrates (see figure 1) combined with reference-free analysis (section 3.2).

In figure 15 we show a THz-TDS conductivity map of a 26 × 42 cm^2 sample of graphene on PEN substrate. The sample is made by transferring individual 10 × 10 cm^2 samples into an array with overlapping regions as clearly seen in figure 15(a). This arrangement leads to patches of SLG with bands of two-layer and squares of four-layer graphene at the intersections. The conductivity clearly increases with increasing number of graphene layers as also shown in the bar plot in figure 15(b). The conductivity map of the graphene on PEN sample reveals many scratches and defects. As it turns out, all the scratches reside in the PEN substrate on the opposite side of the graphene — since they are relatively large and deep, they scatter the THz radiation before reaching the THz detector for those measurement points, which interferes with the determination of the graphene conductivity. Therefore, the quality and handling of the substrate must also be taken into consideration when designing a THz-TDS

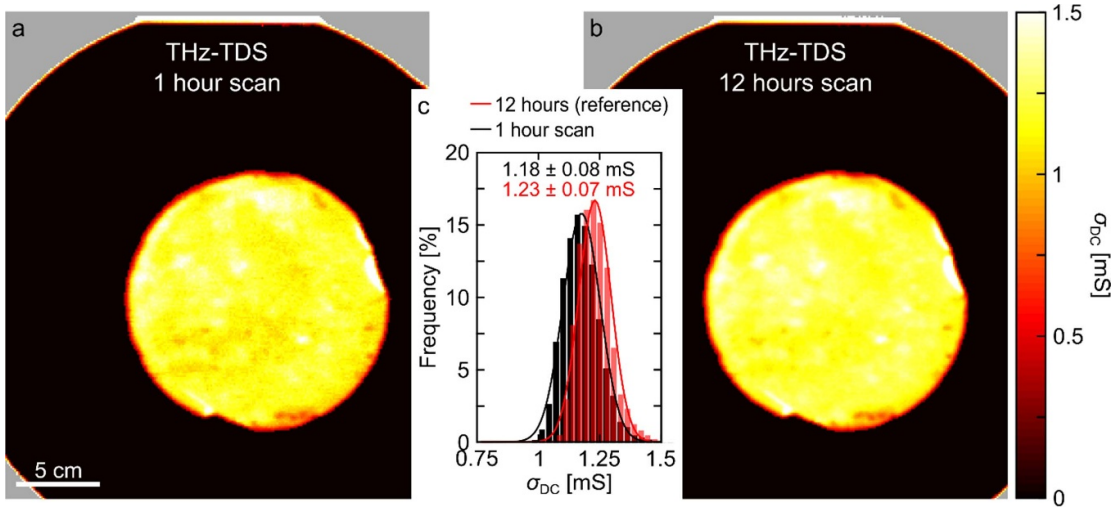


Figure 12. (a), (b) THz-TDS conductivity maps of graphene on 12 inch HR-Si wafer. The maps show results from measuring the same sample in (a) 1 h and (b) 12 h. (c) Histogram of σ_{DC} for the central region of both maps.

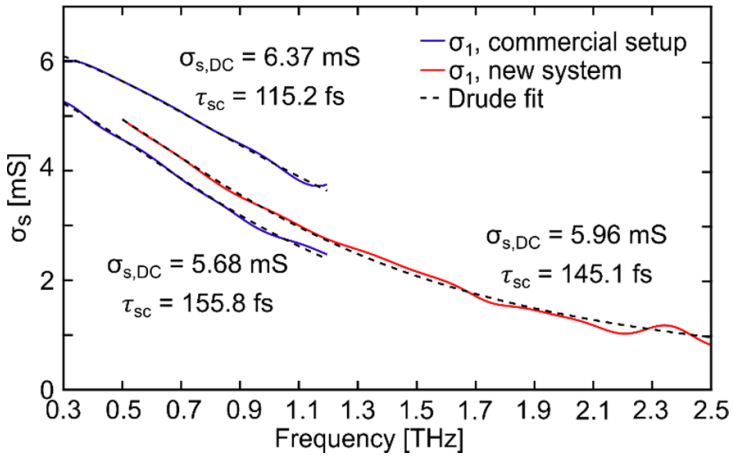


Figure 13. Comparison of THz-TDS frequency-dependent conductivity of graphene on SiC measured with the commercial setup used for most results presented in this work and a newer commercial setup with larger bandwidth and higher data acquisition rate. Reprinted with permission from [9] Elsevier.

setup for graphene production scenarios. Nevertheless, THz-TDS is uniquely capable of detecting defects in graphene not immediately visible for optical inspection [11].

The adaption of THz-TDS into a R2R production line could be based on a THz transmitter and receiver mechanically scanning back and forth across the graphene roll, perpendicular to the roll direction, but a more ideal solution would probably be to base it on fixed THz imaging scanners if proper resolution limits can be reached.

3.5.3. A new IEC metrology standard

As described above and in many other studies, the THz-TDS technique is useful for conductivity mapping of graphene and other conductive thin films. However, for a more accepted use for quality control and documentation in the industry, it is imperative that a broadly accepted measurement protocol is established. Only by standardization will it be possible to compare results from different laboratories and production environments, and thereby to unfold the full potential of the technique. Based on the extensive volume of THz-TDS-based conductivity mapping of graphene that is now available in the literature, we and other partners in the EU Graphene Flagship have therefore developed a new international metrology standard for measurement of the conductivity of graphene under the auspices of the International Electrotechnical Commission (IEC). The standard, IEC TS 62607-6-10, has passed the approval phase of the EU Graphene Flagship and is expected to be published by the IEC in 2021.

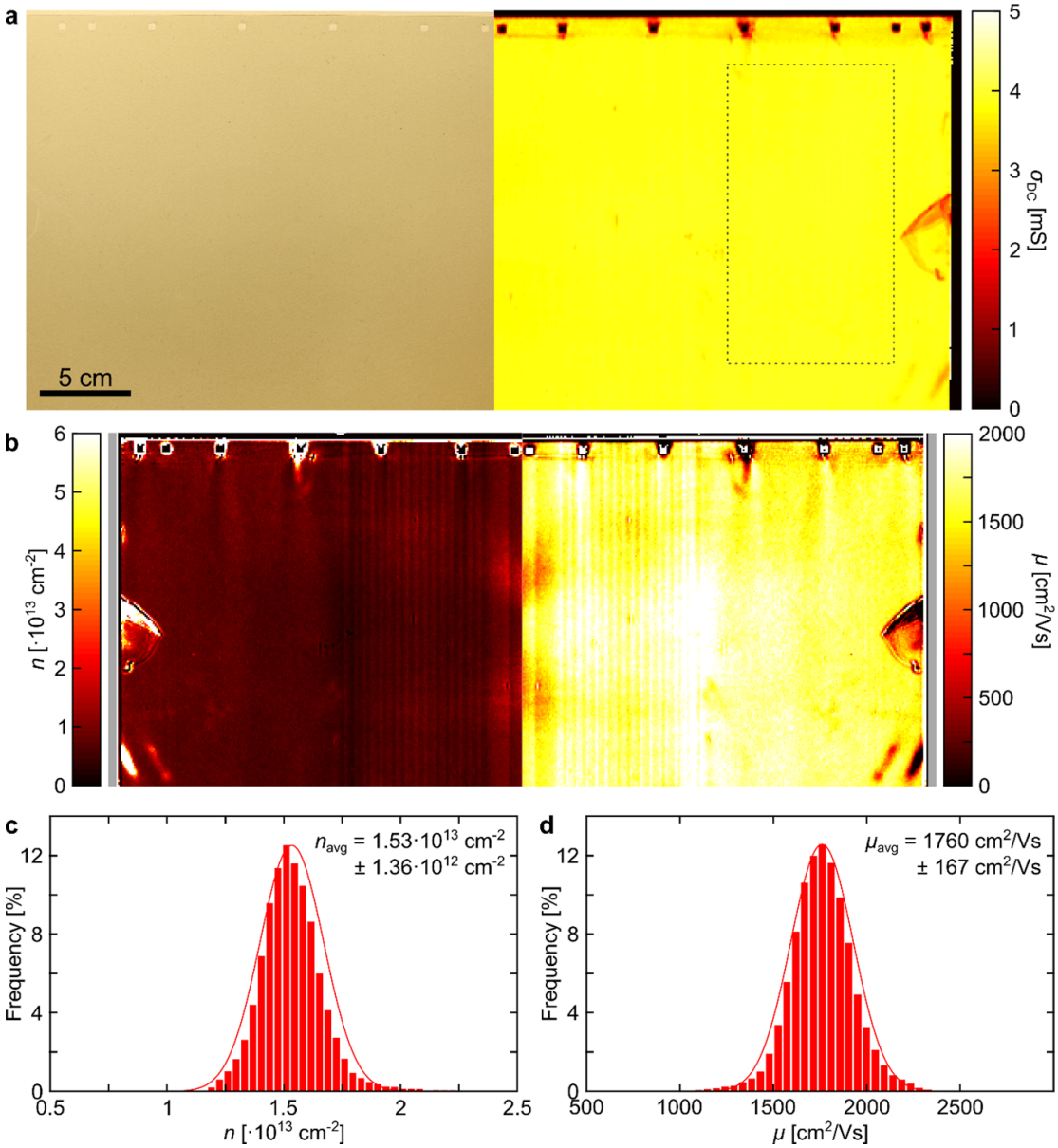


Figure 14. (a) Photograph of 25 × 30 cm^2 graphene on PET sample combined with the THz-TDS conductivity map (mirrored). (b) Maps of n and μ extracted from the THz-TDS measurement of the sample shown in (a). (c), (d) Histograms of (c) n and (d) μ shown together with a fitted normal distribution. The dotted square in (a) highlights the ∼17 500 measurement points used for extracting n and μ for the histograms in (c), (d). (a) Reprinted with permission from [11] The Optical Society.

4. Discussion

We have provided an overview of different cases where THz-TDS proves useful for characterizing the electrical properties of graphene across a wide range of substrates, as well as different types and qualities of graphene. THz-TDS can provide large-area spatial maps of electrical key performance indicators for graphene which we find to be relevant in graphene production scenarios for both batch and R2R production.

There are still obstacles to overcome for integration of THz-TDS in graphene pilot or production lines compared to a well-controlled laboratory environment where instrument down-time, measurement variabilities and artefacts can be dealt with effectively, as throughput is not an issue, and the experimental setup is located in an electrically and mechanically quiet environment. Such obstacles include long term stability of the THz-TDS metrology system and the reproducibility of measurements linked to this. In the case studies presented within this review, we find an overall good reproducibility of results when re-measuring samples over a short time scale (days), while over longer time scales the electrical properties measured from graphene changes due to environmental conditions. In a real-world production line, one would also have to address vibrational disturbances and mechanical drift that could lead to phase errors. Such vibrations could originate from other processes in the production environment that cannot be eliminated easily through mechanical

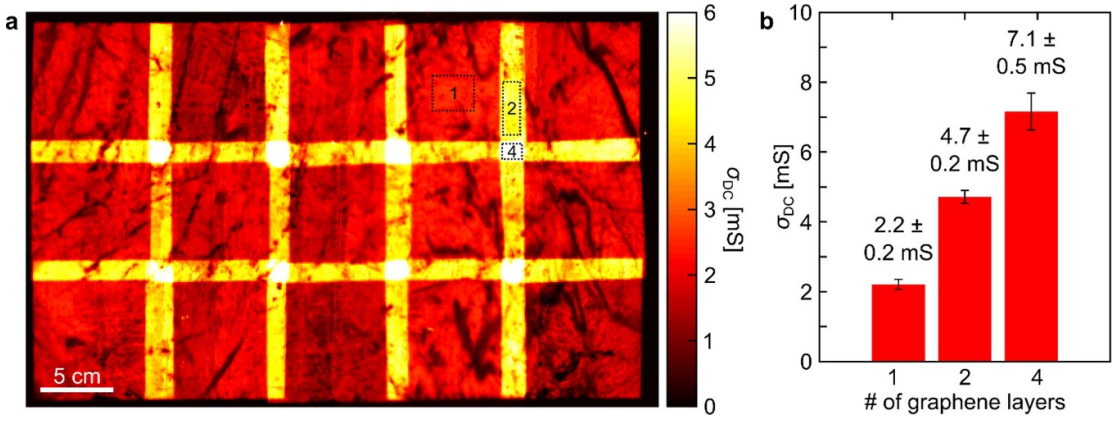


Figure 15. (a) THz-TDS conductivity map of tiled graphene samples on PEN. The total sample area is 26 × 42 cm^2. (b) Bar plot of the σ_{DC} values (average ± standard deviation from fit to normal distribution) from the measurement pixels within the rectangles highlighted on map in (a).

insulation, or for instance from mechanical rollers in a R2R setup where the THz-TDS instrument itself is mounted. Another challenge is reflection mode measurements; these are highly desirable due to the lower price and simpler construction, better performance on non-transparent (terahertz absorbing) substrates and thereby greater utility and convenience. Reflection-based measurements are far more sensitive to variations in probe-sample distance than transmission measurements, and inherently more inaccurate for determination of carrier density and mobility of graphene. There are viable commercial solutions on the market now for inspection of graphene and other thin films (i.e. Das-Nano), but more work needs to be done to bring up reflection-based measurements to the same high standard as transmission measurements. Variations in probe-sample distance are also more critical when moving from far-field transmission mode (as in this paper) towards near-field measurements, which improves the spatial resolution from hundreds of μm to few μm [46]. Commercial near-field THz-TDS setups are also readily available from for instance Protemics GmbH, which offer down to 10–50 μm resolution on continuous graphene samples. The development of scattering-type scanning near-field microscopy (s-SNOM, e.g. from Neaspec) setups operating at THz frequencies that can bring the spatial resolution down to tens of nm is also expected to contribute to the understanding of non-Drude THz spectra in the future. While primarily being research tools due to their slow speed and greater complexity of operation, such instruments could be highly valuable for R&D and diagnostics.

The occurrence of non-Drude like features in the frequency dependent conductivity spectrum for THz-TDS measurements of graphene must also be further investigated. Here, we have used the phenomenological Drude–Smith model (see section 2.2) to determine σ_{DC}, which yields results that compares well to M4PP measurements in section 3.1. There is, however, a lacking fundamental understanding of the link between a measured non-Drude spectrum and the physical appearance of the graphene sample (defects, grain boundaries, local contaminants, etc) and a variety of different models are being developed in the field [15, 66–70]. The use of Monte Carlo simulations is a possible route to reconcile the measurements with an analytical understanding, which is subject to further work.

By addressing these obstacles, the road to integration of THz-TDS into graphene production setups will be cleared, allowing contactless, accurate measurements of the key electrical properties for optimization of graphene growth, transfer, and post-transfer processes.

Acknowledgments

This work was partially funded by the European Union Graphene Flagship under Grant Agreement Nos. 785219 (Core 2) and 881603 (Core 3); Danish National Research Foundation Center for Nanostructured Graphene (DNRF103); European Union Horizon 2020 Research and Innovation Programme under Grant Agreement No. 824962 (car2TERA); European Union Seventh Framework Programme (FP7) under grant Agreement No. 604000 (GLADIATOR); Institute for Basic Science (IBS-R019-D1); National Nature Science Foundation of China (NSFC, Grants Nos. 51902306); Natural Science Pioneer Science Foundation of Chongqing of China (cstc2019jcyj—xfkxX0006).

We acknowledge help with OLED fabrication from Beatrice Beyer and David Wynands (Fraunhofer FEP).

ORCID iDs

Patrick R Whelan https://orcid.org/0000-0002-3978-7029

Abhay Shivayogimath https://orcid.org/0000-0002-5152-0327
David M A Mackenzie https://orcid.org/0000-0003-1114-2955
Bruno Dlubak https://orcid.org/0000-0001-5696-8991
Birong Luo https://orcid.org/0000-0003-0270-0417
Cedric Huyghebaert https://orcid.org/0000-0001-6043-7130
Stiven Forti https://orcid.org/0000-0002-8939-3175
Camilla Coletti https://orcid.org/0000-0002-8134-7633
Alba Centeno https://orcid.org/0000-0001-8442-2283
Peter Bøggild https://orcid.org/0000-0002-4342-0449

References

[1] Backes C *et al* 2020 Production and processing of graphene and related materials *2D Mater.* **7** 022001
[2] Horng J *et al* 2011 Drude conductivity of Dirac fermions in graphene *Phys. Rev.* B **83** 1–5
[3] Tomaino J L, Jameson A D, Kevek J W, Paul M J, Zande A M, van der Barton R A, McEuen P L, Minot E D and Lee Y-S 2011 Terahertz imaging and spectroscopy of large-area single-layer graphene *Opt. Express* **19** 141–6
[4] Maeng I, Lim S, Chae S J, Lee Y H, Choi H and Son J H 2012 Gate-controlled nonlinear conductivity of Dirac fermion in graphene field-effect transistors measured by terahertz time-domain spectroscopy *Nano Lett.* **12** 551–5
[5] Buron J D *et al* 2012 Graphene conductance uniformity mapping *Nano Lett.* **12** 5074–81
[6] Buron J D, Mackenzie D M A, Petersen D H, Pesquera A, Centeno A, Bøggild P, Zurutuza A and Jepsen P U 2015 Terahertz wafer-scale mobility mapping of graphene on insulating substrates without a gate *Opt. Express* **23** 30721
[7] Jnawali G, Rao Y, Yan H and Heinz T F 2013 Observation of a transient decrease in terahertz conductivity of single-layer graphene induced by ultrafast optical excitation *Nano Lett.* **13** 524–30
[8] Whelan P R *et al* 2018 Electrical homogeneity mapping of epitaxial graphene on silicon carbide *ACS Appl. Mater. Interfaces* **10** 31641–7
[9] Whelan P R, Zhao X, Pasternak I, Strupinski W, Jepsen P U and Bøggild P 2019 Non-contact mobility measurements of graphene on silicon carbide *Microelectron. Eng.* **212** 9–12
[10] Mishra N *et al* 2019 Wafer-scale synthesis of graphene on sapphire: toward fab-compatible graphene *Small* **15** 1904906
[11] Whelan P R *et al* 2018 Conductivity mapping of graphene on polymeric films by terahertz time-domain spectroscopy *Opt. Express* **26** 17748–54
[12] Whelan P R *et al* 2020 Fermi velocity renormalization in graphene probed by terahertz time-domain spectroscopy *2D Mater.* **7** 035009
[13] Ivanov I, Bonn M, Mics Z and Turchinovich D 2015 Perspective on terahertz spectroscopy of graphene *Europhys. Lett.* **111** 67001
[14] Bøggild P, Mackenzie D M A, Whelan P R, Petersen D H, Buron J D, Zurutuza A, Gallop J, Hao L and Jepsen P U 2017 Mapping the electrical properties of large-area graphene *2D Mater.* **4** 042003
[15] Kužel P and Němec H 2020 Terahertz spectroscopy of nanomaterials: a close look at charge-carrier transport *Adv. Opt. Mater.* **8** 1900623
[16] Hafez H A, Kovalev S, Tielrooij K, Bonn M, Gensch M and Turchinovich D 2020 Terahertz nonlinear optics of graphene: from saturable absorption to high-harmonics generation *Adv. Opt. Mater.* **8** 1900771
[17] Docherty C J, Parkinson P, Joyce H J, Chiu M-H, Chen C-H, Lee M-Y, Li L-J, Herz L M and Johnston M B 2014 Ultrafast transient terahertz conductivity of monolayer MoS_2 and WSe_2 grown by chemical vapor deposition *ACS Nano* **8** 11147–53
[18] Liu X, Yu H, Ji Q, Gao Z, Ge S, Qiu J, Liu Z, Zhang Y and Sun D 2016 An ultrafast terahertz probe of the transient evolution of the charged and neutral phase of photo-excited electron-hole gas in a monolayer semiconductor *2D Mater.* **3** 014001
[19] Ji J, Zhou S, Wang W, Ling F and Yao J 2019 Active control of terahertz plasmon-induced transparency in the hybrid metamaterial/monolayer MoS_2/Si structure *Nanoscale* **11** 9429–35
[20] Shivayogimath A *et al* 2019 A universal approach for the synthesis of two-dimensional binary compounds *Nat. Commun.* **10** 2957
[21] Tarekegne A T, Zhou B, Kaltenecker K, Iwaszczuk K, Clark S and Jepsen P U 2019 Terahertz time-domain spectroscopy of zone-folded acoustic phonons in 4H and 6H silicon carbide *Opt. Express* **27** 3618
[22] Dai J, Xie X and Zhang X-C 2006 Detection of broadband terahertz waves with a laser-induced plasma in gases *Phys. Rev. Lett.* **97** 103903
[23] Wang T, Iwaszczuk K, Wrisberg E A, Denning E V and Jepsen P U 2016 Linearity of air-biased coherent detection for terahertz time-domain spectroscopy *J. Infrared Millim. Terahertz Waves* **37** 592–604
[24] Strait J H, George P A, Dawlaty J, Shivaraman S, Chandrashekhar M, Rana F and Spencer M G 2009 Emission of terahertz radiation from SiC *Appl. Phys. Lett.* **95** 051912
[25] Grischkowsky D, Keiding S, Van Exter M and Fattinger C 1990 Far-infrared time-domain spectroscopy with terahertz beams of dielectrics and semiconductors *J. Opt. Soc. Am.* B **7** 2006
[26] Whelan P R, Iwaszczuk K, Wang R, Hofmann S, Bøggild P and Jepsen P U 2017 Robust mapping of electrical properties of graphene from terahertz time-domain spectroscopy with timing jitter correction *Opt. Express* **25** 2725
[27] Glover R E and Tinkham M 1957 Conductivity of superconducting films for photon energies between 0.3 and 40 kTc *Phys. Rev.* **108** 243–56
[28] Gorecki J, Klokkou N, Piper L, Mailis S, Papasimakis N and Apostolopoulos V 2020 High-precision THz-TDS via self-referenced transmission echo method *Appl. Opt.* **59** 6744
[29] Whelan P R, Shen Q, Luo D, Wang M, Ruoff R S, Jepsen P U, Bøggild P and Zhou B 2020 Reference-free THz-TDS conductivity analysis of thin conducting films *Opt. Express* **28** 28819
[30] Rehn A, Jahn D, Balzer J C and Koch M 2017 Periodic sampling errors in terahertz time-domain measurements *Opt. Express* **25** 6712
[31] Kužel P, Němec H, Kadlec F, Kadlec C, Kuzel P, Nemec H, Kadlec F and Kadlec C 2010 Gouy shift correction for highly accurate refractive index retrieval in time-domain terahertz spectroscopy *Opt. Express* **18** 15338–48
[32] Sensale-Rodriguez B, Yan R, Liu L, Jena D and Xing H G 2013 Graphene for reconfigurable THz optoelectronics *Proc. IEEE* **101** 1705–16
[33] Buron J D *et al* 2014 Electrically continuous graphene from single crystal copper verified by terahertz conductance spectroscopy and micro four-point probe *Nano Lett.* **14** 6348–55
[34] Strupinski W *et al* 2011 Graphene epitaxy by chemical vapor deposition on SiC *Nano Lett.* **11** 1786–91

[35] Stauber T, Peres N M R and Castro Neto A H 2008 Conductivity of suspended and non-suspended graphene at finite gate voltage *Phys. Rev.* B **78** 085418
[36] Hwang C, Siegel D A, Mo S-K, Regan W, Ismach A, Zhang Y, Zettl A and Lanzara A 2012 Fermi velocity engineering in graphene by substrate modification *Sci. Rep.* **2** 590
[37] González J, Guinea F and Vozmediano M A H 1994 Non-Fermi liquid behavior of electrons in the half-filled honeycomb lattice (A renormalization group approach) *Nucl. Phys.* B **424** 595–618
[38] Das Sarma S, Hwang E H and Tse W-K 2007 Many-body interaction effects in doped and undoped graphene: Fermi liquid versus non-Fermi liquid *Phys. Rev.* B **75** 121406
[39] Stauber T, Parida P, Trushin M, Ulybyshev M V, Boyda D L and Schliemann J 2017 Interacting electrons in graphene: Fermi velocity renormalization and optical response *Phys. Rev. Lett.* **118** 266801
[40] Davies C L, Patel J B, Xia C Q, Herz L M and Johnston M B 2018 Temperature-dependent refractive index of quartz at terahertz frequencies *J. Infrared Millim. Terahertz Waves* **39** 1236–48
[41] Cordon A *et al* 2019 THz to inspect graphene and thin film materials *2019 44th Int. Conf. on Infrared, Millimeter, and Terahertz Waves (IRMMW-THz)* (IEEE) pp 1–2
[42] Mackenzie D M A, Whelan P R, Bøggild P, Jepsen P U, Redo-Sanchez A, Etayo D, Fabricius N and Petersen D H 2018 Quality assessment of terahertz time-domain spectroscopy transmission and reflection modes for graphene conductivity mapping *Opt. Express* **26** 9220–9
[43] Lin H, Braeuninger-Weimer P, Kamboj V S, Jessop D S, Degl'Innocenti R, Beere H E, Ritchie D A, Zeitler J A and Hofmann S 2017 Contactless graphene conductivity mapping on a wide range of substrates with terahertz time-domain reflection spectroscopy *Sci. Rep.* **7** 1–9
[44] Lin H, Burton O J, Engelbrecht S, Tybussek K-H, Fischer B M and Hofmann S 2020 Through-substrate terahertz time-domain reflection spectroscopy for environmental graphene conductivity mapping *Appl. Phys. Lett.* **116** 021105
[45] Pizzocchero F *et al* 2015 Non-destructive electrochemical graphene transfer from reusable thin-film catalysts *Carbon N. Y.* **85** 397–405
[46] Pandey H *et al* 2018 All CVD boron nitride encapsulated graphene FETs with CMOS compatible metal edge contacts *IEEE Trans. Electron Devices* **65** 4129–34
[47] Melios C *et al* 2020 Towards standardisation of contact and contactless electrical measurements of CVD graphene at the macro-, micro- and nano-scale *Sci. Rep.* **10** 3223
[48] Mackenzie D M A, Kalhauge K G, Whelan P R, Østergaard F W, Pasternak I, Strupinski W, Bøggild P, Jepsen P U and Petersen D H 2020 Wafer-scale graphene quality assessment using micro four-point probe mapping *Nanotechnology* **31** 225709
[49] Bøggild P, Grey F, Hassenkam T, Greve D R and Bjørnholm T 2000 Direct measurement of the microscale conductivity of conjugated polymer monolayers *Adv. Mater.* **12** 947–50
[50] Tanikawa T, Matsuda I, Hobara R and Hasegawa S 2003 Variable-temperature micro-four-point probe method for surface electrical conductivity measurements in ultrahigh vacuum *e-Journal Surf. Sci. Nanotechnol.* **1** 50–56
[51] Clarysse T *et al* 2006 Accurate sheet resistance measurement on ultra-shallow profiles *Mater. Res. Soc. Symp. Proc.* **912** 197–202
[52] Petersen D H *et al* 2010 Review of electrical characterization of ultra-shallow junctions with micro four-point probes *J. Vac. Sci. Technol.* B **28** C1C27–33
[53] Walther M, Cooke D G, Sherstan C, Hajar M, Freeman M R and Hegmann F A 2007 Terahertz conductivity of thin gold films at the metal-insulator percolation transition *Phys. Rev.* B **76** 125408
[54] Němec H, Kužel P and Sundström V 2010 Charge transport in nanostructured materials for solar energy conversion studied by time-resolved terahertz spectroscopy *J. Photochem. Photobiol.* A **215** 123–39
[55] Ulbricht R, Hendry E, Shan J, Heinz T F and Bonn M 2011 Carrier dynamics in semiconductors studied with time-resolved terahertz spectroscopy *Rev. Mod. Phys.* **83** 543–86
[56] Joyce H J, Boland J L, Davies C L, Baig S A and Johnston M B 2016 A review of the electrical properties of semiconductor nanowires: insights gained from terahertz conductivity spectroscopy *Semicond. Sci. Technol.* **31** 103003
[57] Luo Y Y, Su F H, Zhang C, Zhong L, Pan S S, Xu S C, Wang H, Dai J M and Li G H 2017 Terahertz transport dynamics in the metal-insulator transition of V 2 O 3 thin film *Opt. Commun.* **387** 385–9
[58] Isacsson A, Cummings A W, Colombo L, Colombo L, Kinaret J M and Roche S 2017 Scaling properties of polycrystalline graphene: a review *2D Mater.* **4** 012002
[59] Yao W, Wu B and Liu Y 2020 Growth and grain boundaries in 2D materials *ACS Nano* **14** 9320–46
[60] Smith N 2001 Classical generalization of the Drude formula for the optical conductivity *Phys. Rev.* B **64** 1–6
[61] Cooke D G, Meldrum A and Uhd Jepsen P 2012 Ultrabroadband terahertz conductivity of Si nanocrystal films *Appl. Phys. Lett.* **101** 1–5
[62] Dadrasnia E, Lamela H, Kuppam M B, Garet F and Coutaz J-L 2014 Determination of the DC electrical conductivity of multiwalled carbon nanotube films and graphene layers from noncontact time-domain terahertz measurements *Adv. Condens. Matter Phys.* **2014** 1–6
[63] Pasternak I, Wesolowski M, Jozwik I, Lukosius M, Lupina G, Dabrowski P, Baranowski J M and Strupinski W 2016 Graphene growth on Ge(100)/Si(100) substrates by CVD method *Sci. Rep.* **6** 21773
[64] Pasternak I, Dabrowski P, Ciepielewski P, Kolkovsky V, Klusek Z, Baranowski J M and Strupinski W 2016 Large-area high-quality graphene on Ge(001)/Si(001) substrates *Nanoscale* **8** 11241–7
[65] Ciuk T, Pasternak I, Krajewska A, Sobieski J, Caban P, Szmidt J and Strupinski W 2013 Properties of chemical vapor deposition graphene transferred by high-speed electrochemical delamination *J. Phys. Chem.* C **117** 20833–7
[66] Shimakawa K, Itoh T, Naito H and Kasap S O 2012 The origin of non-Drude terahertz conductivity in nanomaterials *Appl. Phys. Lett.* **100** 132102
[67] Lovrinčić R 2013 Comment on 'The origin of non-Drude terahertz conductivity in nanomaterials' [Appl. Phys. Lett. 100, 132102 (2012)] *Appl. Phys. Lett.* **102** 096101
[68] Shimakawa K, Itoh T, Naito H and Kasap S O 2013 Response to "Comment on 'The origin of non-Drude terahertz conductivity in nanomaterials'" [Appl. Phys. Lett. 102, 096101 (2013)] *Appl. Phys. Lett.* **102** 096102
[69] Cocker T L, Baillie D, Buruma M, Titova L V, Sydora R D, Marsiglio F and Hegmann F A 2017 Microscopic origin of the Drude-Smith model *Phys. Rev.* B **96** 205439
[70] Ostatnický T, Pushkarev V, Němec H and Kužel P 2018 Quantum theory of terahertz conductivity of semiconductor nanostructures *Phys. Rev.* B **97** 085426
[71] Cultrera A *et al* 2019 Mapping the conductivity of graphene with electrical resistance tomography *Sci. Rep.* **9** 10655
[72] Boll M, Lotz M R, Hansen O, Wang F, Kjær D, Bøggild P and Petersen D H 2014 Sensitivity analysis explains quasi-one-dimensional current transport in two-dimensional materials *Phys. Rev.* B **90** 245432
[73] Lotz M R, Boll M, Hansen O, Kjær D, Bøggild P and Petersen D H 2014 Revealing origin of quasi-one dimensional current transport in defect rich two dimensional materials *Appl. Phys. Lett.* **105** 053115
[74] Lotz M R, Boll M, Østerberg F W, Hansen O and Petersen D H 2016 Mesoscopic current transport in

two-dimensional materials with grain boundaries: four-point probe resistance and Hall effect *J. Appl. Phys.* **120** 134303
[75] Jessen B S, Whelan P R, Mackenzie D M A, Luo B, Thomsen J D, Gammelgaard L, Booth T J and Bøggild P 2018 Quantitative optical mapping of two-dimensional materials *Sci. Rep.* **8** 6381
[76] Dai J, Zhang J, Zhang W and Grischkowsky D 2004 Terahertz time-domain spectroscopy characterization of the far-infrared absorption and index of refraction of high-resistivity, float-zone silicon *J. Opt. Soc. Am.* B **21** 1379
[77] Luo D *et al* 2019 Adlayer-free large-area single crystal graphene grown on a Cu(111) foil *Adv. Mater.* **31** 1903615
[78] Yu Q *et al* 2011 Control and characterization of individual grains and grain boundaries in graphene grown by chemical vapour deposition *Nat. Mater.* **10** 443–9
[79] Huang P Y *et al* 2011 Grains and grain boundaries in single-layer graphene atomic patchwork quilts *Nature* **469** 389–92
[80] Huang M *et al* 2018 Highly oriented monolayer graphene grown on a Cu/Ni(111) alloy foil *ACS Nano* **12** 6117–27
[81] Li B-W, Luo D, Zhu L, Zhang X, Jin S, Huang M, Ding F and Ruoff R S 2018 Orientation-dependent strain relaxation and chemical functionalization of graphene on a Cu(111) foil *Adv. Mater.* **30** 1706504
[82] Nguyen V L *et al* 2015 Seamless stitching of graphene domains on polished copper (111) foil *Adv. Mater.* **27** 1376–82
[83] Zhang J, Lin L, Jia K, Sun L, Peng H and Liu Z 2020 Controlled growth of single-crystal graphene films *Adv. Mater.* **32** 1903266
[84] Xu X *et al* 2017 Ultrafast epitaxial growth of metre-sized single-crystal graphene on industrial Cu foil *Sci. Bull.* **62** 1074–80
[85] Huang M *et al* 2020 Large-area single-crystal AB-bilayer and ABA-trilayer graphene grown on a Cu/Ni(111) foil *Nat. Nanotechnol.* **15** 289–95
[86] Jin S *et al* 2018 Colossal grain growth yields single-crystal metal foils by contact-free annealing *Science* **362** 1021–5
[87] Levesque P L, Sabri S S, Aguirre C M, Guillemette J, Siaj M, Desjardins P, Szkopek T and Martel R 2011 Probing charge transfer at surfaces using graphene transistors *Nano Lett.* **11** 132–7
[88] Gammelgaard L, Caridad J M, Cagliani A, Mackenzie D M A, Petersen D H, Booth T J and Bøggild P 2014 Graphene transport properties upon exposure to PMMA processing and heat treatments *2D Mater.* **1** 035005
[89] Dean C R *et al* 2010 Boron nitride substrates for high-quality graphene electronics *Nat. Nanotechnol.* **5** 722–6
[90] Jandhyala S *et al* 2012 Atomic layer deposition of dielectrics on graphene using reversibly physisorbed ozone *ACS Nano* **6** 2722–30
[91] Sagade A A, Neumaier D, Schall D, Otto M, Pesquera A, Centeno A, Elorza A Z and Kurz H 2015 Highly air stable passivation of graphene based field effect devices *Nanoscale* **7** 3558–64
[92] Mzali S *et al* 2016 Stabilizing a graphene platform toward discrete components *Appl. Phys. Lett.* **109** 253110
[93] Wang L *et al* 2013 One-dimensional electrical contact to a two-dimensional material *Science* **342** 614–7
[94] Emtsev K V *et al* 2009 Towards wafer-size graphene layers by atmospheric pressure graphitization of silicon carbide *Nat. Mater.* **8** 203–7
[95] Lindvall N, Cole M T and Yurgens A 2011 Large-area uniform graphene-like thin films grown by chemical vapor deposition directly on silicon nitride *Appl. Phys. Lett.* **98** 252107
[96] Sun J, Lindvall N, Cole M T, Wang T, Booth T J, Bggild P, Teo K B K, Liu J and Yurgens A 2012 Controllable chemical vapor deposition of large area uniform nanocrystalline graphene directly on silicon dioxide *J. Appl. Phys.* **111** 044103
[97] Chen Z, Qi Y, Chen X, Zhang Y and Liu Z 2019 Direct CVD growth of graphene on traditional glass: methods and mechanisms *Adv. Mater.* **31** 1803639
[98] Whelan P R *et al* 2017 Raman spectral indicators of catalyst decoupling for transfer of CVD grown 2D materials *Carbon N. Y.* **117** 75–81
[99] Luo D *et al* 2017 Role of graphene in water-assisted oxidation of copper in relation to dry transfer of graphene *Chem. Mater.* **29** 4546–56
[100] Verguts K *et al* 2017 Controlling water intercalation is key to a direct graphene transfer *ACS Appl. Mater. Interfaces* **9** 37484–92
[101] Shivayogimath A *et al* 2019 Do-it-yourself transfer of large-area graphene using an office laminator and water *Chem. Mater.* **31** 2328–36
[102] Das A *et al* 2008 Monitoring dopants by Raman scattering in an electrochemically top-gated graphene transistor *Nat. Nanotechnol.* **3** 210–5
[103] Lee J E, Ahn G, Shim J, Lee Y S and Ryu S 2012 Optical separation of mechanical strain from charge doping in graphene *Nat. Commun.* **3** 1024
[104] Rajab K Z, Naftaly M, Linfield E H, Nino J C, Arenas D, Tanner D, Mittra R and Lanagan M 2008 Broadband dielectric characterization of aluminum oxide (Al_2O_3) *J. Microelectron. Electron. Packag.* **5** 2–7
[105] Mackenzie D M A, Buron J D, Bøggild P, Jepsen P U and Petersen D H 2016 Contactless graphene conductance measurements: the effect of device fabrication on terahertz time-domain spectroscopy *Int. J. Nanotechnol.* **13** 591
[106] Gopalan K K, Paulillo B, Mackenzie D M A, Rodrigo D, Bareza N, Whelan P R, Shivayogimath A and Pruneri V 2018 Scalable and tunable periodic graphene nanohole arrays for mid-infrared plasmonics *Nano Lett.* **18** 5913–8
[107] Rahimi S, Tao L, Chowdhury S F, Park S, Jouvray A, Buttress S, Rupesinghe N, Teo K and Akinwande D 2014 Toward 300 mm wafer-scalable high-performance polycrystalline chemical vapor deposited graphene transistors *ACS Nano* **8** 10471–9
[108] Dietz R J B, Vieweg N, Puppe T, Zach A, Globisch B, Göbel T, Leisching P and Schell M 2014 All fiber-coupled THz-TDS system with kHz measurement rate based on electronically controlled optical sampling *Opt. Lett.* **39** 6482
[109] Yahyapour M, Jahn A, Dutzi K, Puppe T, Leisching P, Schmauss B, Vieweg N and Deninger A 2019 Fastest thickness measurements with a terahertz time-domain system based on electronically controlled optical sampling *Appl. Sci.* **9** 1283
[110] Bae S *et al* 2010 Roll-to-roll production of 30-inch graphene films for transparent electrodes *Nat. Nanotechnol.* **5** 574–8
[111] Kobayashi T *et al* 2013 Production of a 100-m-long high-quality graphene transparent conductive film by roll-to-roll chemical vapor deposition and transfer process *Appl. Phys. Lett.* **102** 1–5